Journal of Computational Physics 554 (2026) 114759

Contents lists available at ScienceDirect

Journal of Computational Physics

journal homepage: www.elsevier.com/locate/jcp

Hybrid resolved-unresolved CFD-DEM framework for multiscale fluid-particle systems with irregular-shaped and polydisperse particles

Zhengshou Lai [a,b,c], Shuai Huang [b], Yong Kong [d], Shiwei Zhao [d], Jidong Zhao [d,*], Linchong Huang [a,b,c,*]

[a] School of Civil Engineering, Sun Yat-sen University, 510275, Guangzhou, China
[b] State Key Laboratory of Tunnel Engineering, 510275, Guangzhou, China
[c] Guangdong Key Laboratory of Marine Civil Engineering, School of Civil Engineering, Sun Yat-Sen University, 510275, Guangzhou, China
[d] Department of Civil and Environmental Engineering, The Hong Kong University of Science and Technology, Hong Kong, China

ARTICLE INFO

Keywords:
CFD-DEM
Resolved
Unresolved
Irregular shapes
Signed distance field

ABSTRACT

This study presents a hybrid resolved and unresolved computational fluid dynamics-discrete element method (CFD-DEM) coupling framework for modeling fluid-particle systems involving irregularly shaped and polydisperse particles. The framework integrates high-fidelity signed distance field (SDF) representations for coarse particles with efficient coarse-fine contact algorithms and unresolved or semi-resolved fluid-particle interaction schemes for fine particles. Key features such as accurate representation of irregularly shaped particles, consideration of varying particle sizes, and evaluation of fluid-particle interactions in complex granular settings are highlighted. The hybrid CFD-DEM solver is implemented and verified through a series of standard benchmark tests. A detailed filtration example is provided to demonstrate its capability in modeling multiscale fluid-particle interactions and in analyzing the influence of particle size and shape on filtration behavior. Additional case studies, including channelized sorting, jet-induced destabilization, and dam-break flows, further illustrate the flexibility and effectiveness of the proposed approach in practical applications.

1. Introduction

Fluid-particle systems are of fundamental importance in both natural and engineering contexts, governing key processes such as erosion, sediment transport, and filtration. These systems typically involve multiscale interactions between discrete solid particles and continuum fluid flows, posing substantial challenges for numerical modeling due to the complex couplings in momentum, mass, and energy across scales. Erosion processes, for instance, involve the detachment and transport of fine particles through pore networks formed by coarse granular assemblies. This phenomenon is commonly encountered in geotechnical and environmental applications, including coastal morphodynamics, the stability of underwater structures, and internal erosion in earth dams [1–3]. Coastal erosion, in particular, has emerged as a critical threat to infrastructure resilience and ecological sustainability [4]. Filtration phenomena also present fluid-particle systems of high practical relevance. In granular media filtration, as widely used in water treatment, oil and gas recovery, and industrial solid-liquid separation, particle assemblies often exhibit a broad range of size distributions and complex

---

[*] Corresponding authors.
E-mail addresses: laizhengsh@mail.sysu.edu.cn (Z. Lai), jzhao@ust.hk (J. Zhao), hlinch@mail.sysu.edu.cn (L. Huang).

https://doi.org/10.1016/j.jcp.2026.114759
Received 17 June 2025; Received in revised form 2 January 2026; Accepted 3 February 2026

irregular shapes [5–8]. Fine particles may clog pore throats, alter flow regimes, or impair system performance [9]. Therefore, a robust and accurate modeling framework capable of resolving fluid-particle interactions in geometrically and compositionally heterogeneous media is essential for predicting system behavior and informing design practices.

To simulate such systems, the coupled computational fluid dynamics-discrete element method (CFD-DEM) has become a widely adopted approach [10,11]. Existing CFD-DEM methods could be typically categorized as unresolved or resolved based on the degree to which particle-scale flow structures are captured in the fluid solver. In unresolved approaches, particle-fluid interactions are commonly modeled using empirical interphase exchange laws, such as drag correlations, evaluated from locally averaged or filtered fluid fields [12–15]. In classical cell-based implementations, the fluid mesh is often selected to be on the order of the particle diameter or larger, primarily to maintain numerical robustness and stable evaluation of fluid-particle interactions. This choice helps avoid strong discontinuities when mapping particle volume fractions and momentum source terms onto control volumes. However, this practice should be regarded as a pragmatic convention rather than an inherent requirement of the unresolved formulation. In contrast, resolved CFD-DEM methods explicitly resolve the flow around individual particles using techniques such as body-fitted arbitrary Lagrangian-Eulerian (ALE) methods [16] or immersed boundary (IB) methods [17]. ALE methods track particle motion via deformable meshes, but suffer from mesh distortion under large deformations and typically require remeshing. IB methods embed particles within a fixed Eulerian grid and enforce no-slip and impenetrability conditions through source forces or strongly imposed constraints, offering enhanced robustness and flexibility for moving and complex geometries [18–23]. While such resolved methods provide high-fidelity descriptions of particle-scale flow structures, their substantial computational cost limits their application to relatively small systems or idealized configurations, making them impractical for many engineering-scale problems.

To bridge the gap between resolved and traditional unresolved methods, a class of semi-resolved CFD-DEM formulations has emerged in recent years [24–30]. In this study, the term semi-resolved refers to Euler-Lagrange formulations in which the interphase coupling terms and flow variables entering drag laws are reconstructed or regularized over a local neighborhood, rather than being extracted solely from the host cell. A key direction involves volume-filtered formulations, where the governing equations are defined at a prescribed filter scale and the interphase momentum exchange is regularized using a kernel with a width decoupled from the mesh resolution. This allows consistent convergence under grid refinement at fixed filter scale [31–33]. Closely related ideas are also realized in volume-averaging schemes, where the averaging volume is independent of the mesh control volumes. This reduces discontinuities introduced by cell-centered mappings between particle and fluid fields. A representative example is the quadrature-centered averaging scheme, which evaluates void fraction at quadrature points using a volume-averaging sphere that may extend beyond the host element [34]. From an implementation perspective, many semi-resolved methods reconstruct the flow variables required by closure models via kernel-based interpolations over neighboring cells. This enhances robustness and provides greater flexibility in handling polydisperse particle systems [24–26]. Despite these advances, such methods remain within the unresolved category, as they rely on empirical interphase exchange models. Their predictive performance still hinges on closure accuracy. In particular, once the filter or averaging scale is treated as a modeling parameter independent of the mesh, a central challenge arises in reconstructing the undisturbed fluid velocity from the filtered or averaged velocity field [35].

It is also worthwhile noting the two-fluid models (TFM) which offer an alternative by treating both phases as interpenetrating continua, governed by separate conservation equations and coupled through interphase momentum exchange terms [36–39]. Compared to CFD-DEM, TFM offers significantly reduced computational cost, making it attractive for large-scale or industrial-scale simulations. However, the accuracy of TFM critically depends on the closure relations, particularly the constitutive models for the particle-phase stress tensor and interphase momentum exchange relations. These closures are often derived under simplifying assumptions such as spherical particle geometry, monodispersity, and homogeneous flow fields, which limit their predictive capability in more complex scenarios.

To address the above limitations on modeling fluid-particle interactions involving irregular shaped and polydisperse particles, recent efforts have focused on developing hybrid CFD-DEM frameworks that integrate resolved and unresolved schemes. This paradigm leverages the accuracy of locally resolved solvers while maintaining global computational tractability. Pioneering recent studies on this hybrid framework include works by Kuruneru et al. [40], Wang et al. [41], Xie et al. [42], Hu et al. [43], and etc. For instance, Xie et al. [42] proposed a hybrid CFD-DEM approach incorporating resolved, semi-resolved, and unresolved schemes within a fictitious domain framework to simulate interactions between fluids and coarse, medium, and fine particles. Although this strategy improves modeling accuracy and applicability across diverse particle size distributions, it remains largely limited to spherical particles. To address this constraint, Hu et al. [43] extended the hybrid framework by employing a clump-based representation to model irregular-shaped particles. While this approach improves geometric fidelity compared to spherical models, it often requires a large number of convex primitives and struggles to accurately capture surface curvature, leading to increased computational cost and limited applicability of curvature-based contact models [44]. To overcome these limitations, recent advances in discrete element modeling have introduced signed distance field (SDF) methods, which enable continuous and accurate representations of arbitrarily shaped particles [44–47]. The integration of SDF-based DEM with CFD presents a promising pathway toward a unified hybrid resolved-unresolved CFD-DEM framework capable of capturing complex fluid-particle interactions with enhanced geometric versatility and multiscale consistency.

Building upon this foundation, the present study develops a hybrid resolved-unresolved CFD-DEM framework incorporating SDF-based particle representation to simulate fluid-particle interactions involving irregularly shaped and polydisperse particles. The main contributions are threefold. First, a unified numerical framework is established by coupling SDF-based DEM with both resolved and unresolved CFD schemes, enabling consistent treatment of particle geometry, contact mechanics, and fluid coupling across scales. Second, an efficient contact algorithm is proposed within the SDF framework to robustly handle interactions between coarse and fine particles, supporting scalable simulation of multiscale granular systems. Third, the proposed framework is applied to a series

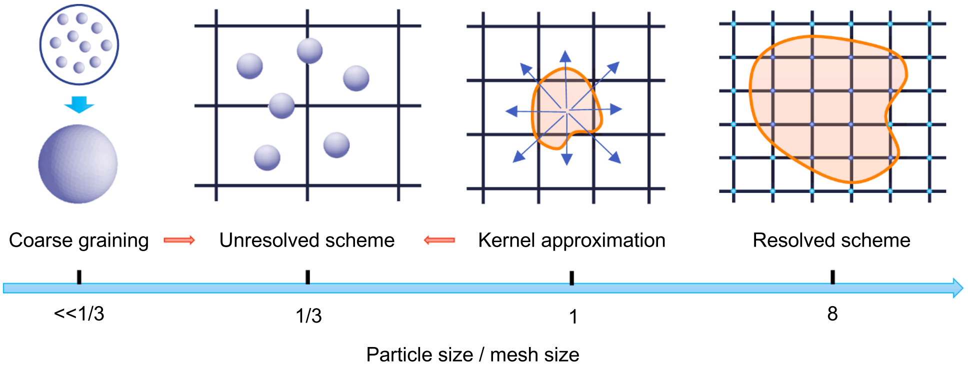

Fig. 1. Overview of the various schemes of resolving fluid-particle interaction and their adaptable realms.

of representative problems, including a detailed case study of fine particle filtration through coarse granular media and several extended examples such as granular sorting in channels, jet induced by destabilization and dam-break flow. These examples collectively demonstrate the applicability and effectiveness of the method in complex geotechnical and environmental settings. It is noted that SDF representations have also been adopted in IB formulations to provide accurate level-set geometry descriptions for resolved flow computations, including sharp-interface and discrete-forcing approaches [23,48,49]. These developments indicate that SDF is a viable geometry carrier for resolved CFD-DEM. In the present work, SDF is further integrated into a hybrid resolved-unresolved CFD-DEM framework to enable a consistent treatment of irregular particle geometry and coupling across multiple resolution regimes. To the best of the authors' knowledge, such multiscale particle-fluid systems involving irregular shapes and wide size distributions have not been resolved using high-fidelity numerical tools, and the present study provides a novel and practical computational solution.

The remainder of the paper is organized as follows. Section 2 introduces the overall structure of the hybrid CFD-DEM framework. Section 3 presents the computational methodologies. Section 4 details the implementation and verification. Section 5 discusses a primary case study on filtration through granular media. Section 6 presents additional examples involving granular flows and multiscale interactions. Finally, Section 7 summarizes the key findings and future perspectives.

2. Overview of the framework

An overview of the hybrid CFD-DEM framework and the resolution strategies for fluid-particle interactions is illustrated in Fig. 1. The objective of this framework is to support accurate and efficient modeling across a wide range of particle-to-fluid size ratios, particularly for systems involving irregularly shaped and polydisperse particles. To this end, the framework adaptively selects among three resolution schemes, namely the resolved, semi-resolved, and unresolved, based on the local particle size relative to the characteristic fluid cell size.

Specifically, when the particle size is significantly larger than the fluid cell size (typically exceeding a ratio of 8), the resolved scheme is activated to directly capture the particle-induced flow field. Conversely, when the particle size is much smaller than the fluid cell size (typically below a ratio of 1/3), the unresolved scheme is adopted, relying on drag-based interphase momentum exchange models. For intermediate size ratios (between 1/3 and 8), the semi-resolved scheme is employed, where local flow properties are interpolated over neighboring cells to enhance accuracy without resolving the full disturbance field. It should be noted that these thresholds are not strict boundaries, but rather practical guidelines informed by accumulated modeling experience in single-scheme CFD-DEM approaches [15,50]. In cases where the number of small particles becomes extremely large, coarse-graining may be considered in unresolved CFD-DEM to reduce computational cost [51,52]. Since coarse-graining is not used in the present work, it is not further discussed here.

A critical component of the proposed framework is the use of an SDF-based particle representation, which enables accurate geometric descriptions of irregularly shaped particles. Previous studies introduced SDF-DEM for handling irregular particle geometry and contact detection [44], and later extended it to an IB-based, fully resolved SDF-CFD-DEM framework for simulating non-spherical particles [45]. Building on these developments, the present work advances a hybrid resolved-unresolved CFD-DEM framework featuring unified governing equations and fluid-solid exchange operators, tailored for multiscale systems involving irregularly shaped and polydisperse particles. In parallel, a new point-large particle contact approach is proposed to address coarse-fine interactions in polydisperse media, leveraging the SDF-DEM formalism. In this approach, fine particles are treated as points or spheres, and their contact with coarse SDF-defined particles is computed via a simplified and scalable algorithm. This enhancement facilitates efficient simulation of multiscale granular systems while maintaining contact accuracy. The governing equations and numerical implementation of the SDF-based hybrid CFD-DEM framework are presented in the following section.

3. Methodologies

Most resolution strategies for fluid-particle interaction have been well established in the literature. Therefore, this section provides only a concise summary of the core formulations for completeness, with an emphasis on how these methods are adapted for hybrid coupling across different resolution regimes and extended to accommodate irregularly shaped particles through SDF representations.

3.1. Formulation of CFD

For two-phase fluids commonly encountered in natural and engineering contexts, the continuity and momentum equations [14,45,53], with the consideration of porous media, could be given as

$$\frac{\partial(\epsilon\rho_f)}{\partial t} + \nabla\cdot\left(\epsilon\rho_f\vec{u}_f\right) = 0 \tag{1}$$

$$\frac{\partial(\epsilon\rho_f\vec{u}_f)}{\partial t} + \nabla\cdot(\epsilon\rho_f\vec{u}_f\otimes\vec{u}_f) = -\epsilon\nabla p + \epsilon\nabla\cdot\vec{\tau}_f + \epsilon\rho_f\vec{g} + \vec{f}_t + \vec{f}_p \tag{2}$$

where ρ_f is the fluid density, $\vec{u}_f$ denotes the fluid velocity, and p is the pressure, $\vec{\tau}_f$ is the deviatoric viscous stress tensor. The porosity ϵ accounts for the local volumetric fraction of fluid. The term $\vec{g}$ is gravitational acceleration, $\vec{f}_t$ represents the surface tension force at fluid-fluid interfaces, and $\vec{f}_p$ denotes the interaction force exerted by the particles on the fluid. The latter is computed differently across resolution schemes, depending on the particle-to-mesh size ratio, which will be elaborated in the subsequent subsections.

The volume-of-fluid (VOF) method is employed to capture fluid-fluid interfaces by solving a transport equation for the phase fraction α [54,55]. The mixture density and viscosity are computed via algebraic blending:

$$\rho_f = \alpha\rho_\ell + (1-\alpha)\rho_g \tag{3}$$

$$\mu_f = \alpha\mu_\ell + (1-\alpha)\mu_g \tag{4}$$

where subscripts ℓ and g refer to the liquid and gas phases, respectively. The evolution of the phase-fraction field is governed by

$$\frac{\partial(\epsilon\alpha)}{\partial t} + \nabla\cdot(\epsilon\alpha\vec{u}_f) = 0 \tag{5}$$

where ϵ denotes the local porosity. The combination of Eqs. (1) and (5) ensures global conservation of each phase within a porous control volume. In the limit $\epsilon \equiv 1$, the formulation reduces to the standard VOF system for free flow. To maintain boundedness and preserve interface sharpness, the interface-capturing scheme is enhanced using the multidimensional universal limiter with explicit solution (MULES) algorithm [56].

Surface tension is modeled using the continuum surface force (CSF) approach [55]:

$$\vec{f}_t = \sigma\kappa\nabla\alpha \tag{6}$$

where σ is the surface tension coefficient and κ is the interface curvature, computed from the phase-fraction field as

$$\kappa = -\nabla\cdot\vec{n}, \qquad \vec{n} = \frac{\nabla\alpha}{|\nabla\alpha|} \tag{7}$$

While capillary effects at fluid-solid interfaces, particularly in partially saturated systems, can be significant, they are not considered in the present study. The focus here is on fluid-fluid momentum coupling, and solid-related surface tension will be addressed in future work.

3.2. Formulation of DEM

In DEM, particle motion is governed by the Newton-Euler equation as

$$m\frac{\partial\vec{u}_p}{\partial t} = m\vec{g} + \vec{F}_c + \vec{F}_f \tag{8}$$

$$\vec{I}\frac{\partial\vec{\omega}_p}{\partial t} + \vec{\omega}_p\times(\vec{I}\vec{\omega}_p) = \vec{M}_c + \vec{M}_f \tag{9}$$

where $\vec{u}_p$ and $\vec{\omega}_p$ are particle translation and rotation velocities, m and $\vec{I}$ are particle mass and moment of inertia tensor, and $\vec{F}_c$, $\vec{M}_c$, $\vec{F}_f$, and $\vec{M}_f$ are the contact force, contact moment, fluid force, and force moment experienced by the particle, respectively. It is worthwhile noting the distinction between non-capital $\vec{f}$ used for force in CFD formulation (a force density weighted by volume) and capital $\vec{F}$ used in DEM (total force).

For modeling irregularly-shaped particles, the SDF-DEM [44] recently proposed by the authors is adopted. In brief, SDF-DEM describes particles using an SDF-based generic interface with two functions: the SDF function and surface projection function. The SDF function maps a location to a scalar, assumed positive inside a particle and negative outside, with the zeroth isosurface representing the particle surface. The surface projection function projects a point onto the particle surface to determine the contact point. Using the SDF-based particle description, the node-to-surface contact algorithm detects contacts and resolves contact geometric features. A brief description about the formulation of SDF-DEM is presented in Appendix A. Interested readers are referred to [44,57] for more details.

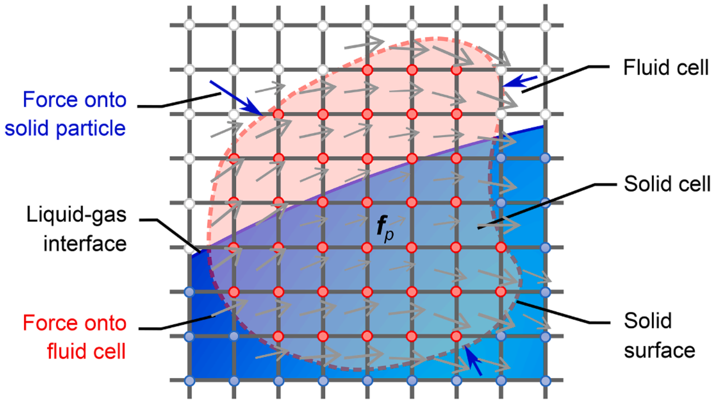

Fig. 2. Illustration of resolved CFD-DEM coupling. Particle boundaries are explicitly resolved by the fluid mesh, and fluid-particle interaction is computed via direct stress integration over particle surfaces.

Remark 1. Flexibility of DEM formulation: While the present study adopts the SDF-DEM to represent irregularly shaped particles, the proposed hybrid CFD-DEM framework is not restricted to this particular DEM formulation. Alternative contact solvers, such as the convex-based Gilbert-Johnson-Keerthi (GJK) method or data-driven machine learning models [58,59], can be readily integrated within the same coupling strategy. In the current implementation, the SDF representation serves to facilitate the mapping of particles onto the Eulerian fluid mesh, enabling efficient evaluation of solid volume fraction and porosity fields. This mapping capability makes SDF particularly advantageous for CFD-DEM coupling, especially in the context of complex geometries or non-convex particle shapes. However, the underlying fluid-particle interaction schemes and the hybrid resolution strategy remain agnostic to the choice of DEM contact solver.

3.3. Resolved fluid-particle interaction

In the resolved regime, the IB method is employed to couple fluid and particle dynamics [17]. Fluid-to-particle forces are obtained by integrating hydrodynamic stresses over particle surfaces, while the particle's influence on the fluid is modeled by introducing a momentum source term in the Navier-Stokes equations [60,61], as illustrated in Fig. 2. In cells partially or fully occupied by solids, the target (corrected) fluid velocity $\hat{\vec{u}}_f$ is defined as a density-weighted mixture of the local fluid velocity and the rigid-body velocity of the particle:

$$\hat{\vec{u}}_f = (1 - \varphi_s)\vec{u}_f + \varphi_s \vec{u}_s \tag{10}$$

$$\vec{u}_s = \vec{u}_p + \vec{\omega}_p \times (\vec{x}_i - \vec{x}_p) \tag{11}$$

where $\varphi_s = \phi_s \rho_s / \rho$ is the density-weighted solid fraction, ϕ_s denotes the geometric solid fraction, and $\rho = (1 - \phi_s)\rho_f + \phi_s \rho_s$ is the mixture density. The quantities $\vec{u}_p$ and $\vec{\omega}_p$ are the translational and angular velocities of the particle, respectively, while $\vec{x}_i$ and $\vec{x}_p$ denote the cell center and particle centroid, respectively [45].

After finite-volume discretization and semi-implicit linearization of the transient, convective, and diffusive terms, the momentum predictor at a given PISO (pressure-implicit splitting of operators) substep takes the following form:

$$A_u \vec{u}_f - \vec{H} = -\epsilon \nabla p + \vec{f}_p \tag{12}$$

where A_u is the diagonal coefficient (with units of mass per time) incorporating the implicit contributions from transient and diffusive operators along with the linearized convection term. The vector $\vec{H}$ collects the explicitly treated terms and known sources at the current substep, including gravity and interfacial tension. The IB forcing term is then defined as

$$\vec{f}_p = A_u \left(\vec{u}_f - \hat{\vec{u}}_f \right) \tag{13}$$

which enforces $\vec{u}_f = \hat{\vec{u}}_f$ upon substitution into Eq. (12). In multi-particle systems, $\vec{f}_p$ should be averaged from all particles overlapping a given cell to conserve local momentum. Practically, each particle contributes its own IB source field, which is counted prior to matrix assembly to avoid overwriting contributions in shared cells.

The hydrodynamic stress divergence used in the formulation is given by

$$\nabla \cdot \vec{\sigma} = -\nabla p + \nabla \cdot (\mu_f \nabla \otimes \vec{u}_f) \tag{14}$$

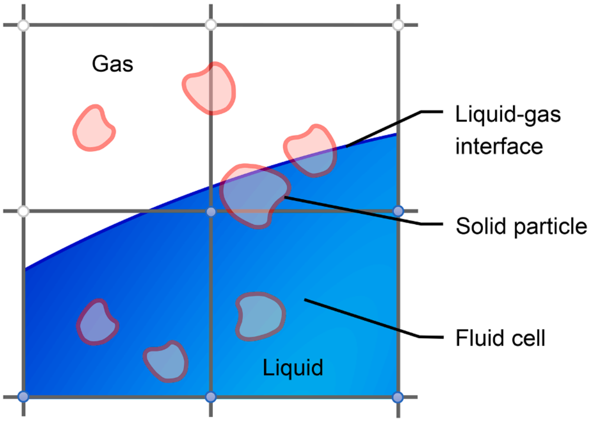

Fig. 3. Illustration of unresolved CFD-DEM coupling. Particles are subgrid-scale, and fluid-particle interaction is modeled using empirical closures (e.g., drag models) based on local flow properties of the fluid cell a particle belongs to.

consistent with the pressure and viscous terms in the CFD formulation. The total hydrodynamic force and torque acting on a particle are computed via volume integration, equivalent to a surface integral by the divergence theorem [45]:

$$\vec{F}_f = \sum^{cells} \left(\varphi_s \nabla \cdot \vec{\sigma} - (1-\varphi_s)\vec{f}_p \right) V_c \tag{15}$$

$$\vec{M}_f = \sum^{cells} (\vec{x}_i - \vec{x}_p) \times \left(\varphi_s \nabla \cdot \vec{\sigma} - (1-\varphi_s)\vec{f}_p \right) V_c \tag{16}$$

where V_c is the cell volume.

It is noted that the current resolved framework does not include an explicit pairwise lubrication correction. Near-contact hydrodynamics are represented through IB coupling at the resolved grid scale, and interparticle overlap is prevented by a soft-sphere contact approach. When lubrication becomes rate-controlling due to narrow gaps, three enhancement strategies are available. The first is a velocity-separation update that exchanges momentum based on predictor-corrector velocities and captures near-contact dissipation without invoking explicit pairwise forces [62]. The second introduces timestep restriction and boundary-layer reconstruction with robust handling of dual-particle cells, recovering lubrication resistance over a finite-gap range [63]. The third involves adding a near-field correction term, either in the form of a calibrated barrier force [64] or using a singular-regular decomposition, wherein the singular lubrication load is applied analytically while the solver resolves only the regular component [65]. In cases where analytic pairwise asymptotics are employed, the near-field term can follow the converging-sphere solutions to capture the leading-order behavior of the small-gap force [66].

3.4. *Unresolved fluid-particle interaction*

In the unresolved regime, fluid-particle interactions are modeled using empirical drag force correlations, as illustrated in Fig. 3. Theoretically, exact expressions exist only for single spherical particles under creeping flow conditions, such as those described by the Stokes-Einstein relation [67]. In practical simulations, correction models are required to account for particle concentration, size, shape, and flow regime. A comprehensive review of such models is available in [68].

In this study, the Gidaspow model [69] is employed, which combines the Ergun equation [70] for dense suspensions and the Wen-Yu model [71] for dilute systems. Specifically, the Ergun term is applied when the fluid volume fraction ϵ is less than 0.8, and the Wen-Yu term is used otherwise. The dimensionless drag factor $\hat{\vec{f}}_{drag}$ is defined as

$$\hat{\vec{f}}_{drag} = \begin{cases} \frac{150(1-\epsilon)}{18\epsilon^2} + \frac{1.75}{18\epsilon^2} Re & \epsilon \le 0.8 \\ \frac{C_d}{24} Re \epsilon^{-3.65} & \epsilon > 0.8 \end{cases} \tag{17}$$

$$C_d = \begin{cases} \frac{24}{Re}\left(1 + 0.15 Re^{0.687}\right) & Re \le 1000 \\ 0.44 & Re > 1000 \end{cases} \tag{18}$$

where Re is the Reynolds' number, and C_d is the drag coefficient. Thereby, the drag force applied on the particles is calculated as

$$\vec{F}_{drag} = \hat{\vec{f}}_{drag} \left(3\pi\epsilon\mu_f d \vec{u}_{rel} \right) \tag{19}$$

where $\vec{u}_{rel} = \vec{u}_p - \vec{u}_f$ is the relative velocity of the particle to the fluid and d is the particle size. The buoyant force is calculated as

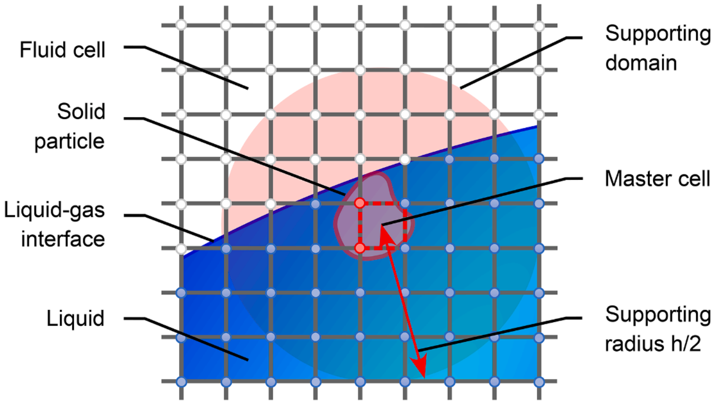

Fig. 4. Illustration of semi-resolved CFD-DEM coupling. Moderately sized particles interact with multiple fluid cells. Fluid properties are interpolated from surrounding cells using a kernel function, and interaction forces are conservatively spread back to the fluid grid.

$$\vec{F}_{buoy} = -V_p \nabla p \tag{20}$$

where V_p is the particle volume. The total source term applied to the fluid from all particles within a control volume is then

$$\vec{f}_p = \frac{1}{V_c} \sum^{p} \left(\vec{F}_{drag} + \vec{F}_{buoy} \right) \tag{21}$$

where $\sum^p$ indicates the summation of all particles within a fluid cell and V_c is the volume of the fluid cell. In the implementation, the drag force is split into an explicit part and an implicit part, respectively, with one corresponding to $\vec{u}_p$ and the other corresponding to $\vec{u}_f$ in Eq. (19). This treatment enhances the convergence rate and numerical stability.

In this framework, shape irregularity of large particles is resolved explicitly using the resolved scheme described earlier. For fine particles treated in the unresolved regime, shape effects are implicitly embedded in the drag coefficient. Although not pursued in this work, shape-dependent drag correlations can be derived through high-fidelity resolved simulations. For instance, synthetic particles with varying morphology descriptors (e.g., elongation, flatness, sphericity, roundness) can be generated using methods such as spherical harmonic expansions [46], and used to construct drag-shape models based on resolved CFD-DEM simulations. It is also noted that the hydrodynamic torque is neglected, and particle rotation in the unresolved regime is driven only by contact interactions. This simplification is reasonable if the fine particles are substantially smaller than the coarse ones, and the target observables are expected to exhibit limited sensitivity to their fluid-induced rotational dynamics. If needed, established torque closures can be incorporated to account for viscous resistance to particle rotation [72]. These directions will be explored in future work.

In addition, explicit lubrication terms are not included in either the unresolved or the semi-resolved schemes in this study. When near-contact hydrodynamics become rate-controlling, lubrication forces may be introduced at the DEM level using analytical or empirical pairwise resistance models for particle-particle and particle-wall interactions. Such corrections are typically activated below a threshold gap and regularized by a small-gap cut-off, with a smooth transition to the contact law to ensure numerical stability and avoid double counting with the resolved flow field [73,74]. Continuous unresolved formulations that account for surface roughness and particle deformation have also been proposed [75]. Within the present hybrid framework, the SDF offers a robust, geometry-aware measure of interparticle gaps, applicable to irregular shapes and multi-contact configurations. This enables activation of DEM-level pairwise lubrication consistently across both unresolved and semi-resolved regimes. Together with the resolved scheme options described in the previous subsection, the framework could provide a unified treatment of lubrication effects across particle sizes and resolution scales.

3.5. Semi-resolved fluid-particle interaction

The semi-resolved CFD-DEM scheme may also be called as the kernel-based approximation approach which is originally proposed for dealing with moderately fine particles [28,29]. For particles with sizes comparable to or even larger than (e.g., 1/3 to 8 times) the size of fluid cells, accurately estimating void fraction and fluid velocity based on a single fluid cell overlapped by the particle becomes challenging. Consequently, the drag force cannot be accurately determined. To address this issue, void fraction and fluid velocity can be interpolated from a set of neighboring fluid cells near the particle, as illustrated in Fig. 4. Additionally, the reaction force from particles to fluids is spread to all neighboring fluid cells. By interpolating fluid properties for drag force calculation and spreading the drag force to neighboring cells, the fluid-particle interaction becomes reasonable for moderately fine particles, allowing the use of the unresolved CFD-DEM approach.

In this work, a compact Peskin-type kernel is adopted for interpolation and spreading [17]. Let d denote the Euclidean distance from a query point to the center of the support domain, and h the support size (diameter). In practice, h could be chosen around

3∼5 particle diameters to balance smoothness and locality. The one-dimensional kernel $\delta(r)$, with normalized coordinate $r = 2d/h$, is defined as

$$\delta(r) = \begin{cases} \frac{1}{8}\left(3 - 2r + \sqrt{1 + 4r - 4r^2}\right), & 0 \le r \le 1 \\ \frac{1}{8}\left(5 - 2r - \sqrt{-7 + 12r - 4r^2}\right), & 1 < r \le 2 \\ 0, & r > 2 \end{cases} \tag{22}$$

and the corresponding three-dimensional kernel is defined in tensor-product form:

$$\delta_h(\vec{x} - \vec{X}) = \delta\left(\frac{2|x-X|}{h}\right)\delta\left(\frac{2|y-Y|}{h}\right)\delta\left(\frac{2|z-Z|}{h}\right) \tag{23}$$

where $\vec{x} = (x, y, z)$ and $\vec{X} = (X, Y, Z)$ are spatial coordinates.

For a particle p whose centroid lies within a master cell $c(p)$ centered at $\vec{x}_c$, define the linked neighbor set $\mathcal{N}(c)$ as the set of all cells j for which $\delta_h(\vec{x}_j - \vec{x}_c) > 0$. The unnormalized and normalized kernel weights are given by

$$W_{cj} = V_j \delta_h(\vec{x}_j - \vec{x}_c), \qquad \omega_{cj} = \frac{W_{cj}}{\sum_{m\in\mathcal{N}(c)} W_{cm}}, \qquad \sum_{j\in\mathcal{N}(c)} \omega_{cj} = 1 \tag{24}$$

where V_j is the volume of cell j. Any Eulerian field ψ is interpolated to the particle location via

$$\tilde{\psi}_p = \sum_{j\in\mathcal{N}(c(p))} \omega_{c(p)j}\psi_j \tag{25}$$

and any particle-based quantity Q_p is conservatively spread to the Eulerian grid as

$$\mathcal{S}_j(Q) = \frac{1}{V_j}\sum_p \omega_{c(p)j} Q_p \tag{26}$$

where $\mathcal{S}_j(Q)$ is the spread quantity. It should be noted that the kernel weights in Eq. (24) are computed using the center of the particle's master fluid cell, rather than the actual particle centroid. This approximation enables the weights to be precomputed and reused across time steps, reducing computational cost without significant loss of accuracy.

Within this kernel-based approximation framework, the solid volume of each particle is similarly distributed to its neighboring cells, yielding a semi-resolved porosity field:

$$V_{p\to j} = \omega_{c(p)j} V_p, \qquad \phi_{s,j} = \min\left(1, \sum_p \frac{V_{p\to j}}{V_j}\right), \qquad \epsilon_j = 1 - \phi_{s,j} \tag{27}$$

Fluid properties at the particle centroid, including velocity $\tilde{\vec{u}}_p$, density $\tilde{\rho}_p$, viscosity $\tilde{\mu}_p$, and porosity $\tilde{\epsilon}_p$, are evaluated using Eq. (25) with $\psi \in \vec{u}_f, \rho_f, \mu_f, \epsilon$.

The net interphase force $\vec{F}_p^{\text{int}}$ acting on particle p (e.g., drag and buoyancy) is computed using the unresolved closures presented earlier but evaluated with the kernel-interpolated properties. The corresponding reaction source to the fluid momentum equation is conservatively spread as:

$$\vec{f}_{p,j} = -\frac{1}{V_j}\sum_p \omega_{c(p)j}\vec{F}_p^{\text{int}}, \qquad \sum_j \vec{f}_{p,j} V_j = -\sum_p \vec{F}_p^{\text{int}} \tag{28}$$

If angular momentum feedback is needed, a torque source term can be added as:

$$\vec{\tau}_j = -\frac{1}{V_j}\sum_p \omega_{c(p)j}(\vec{x}_j - \vec{x}_p) \times \vec{F}_p^{\text{int}} \tag{29}$$

Together, the kernel-based interpolation and conservative spreading described above, particularly Eqs. (25)-(28), constitute the semi-resolved coupling scheme adopted in this study. This scheme ensures global momentum conservation by construction, enhances numerical robustness for moderately fine particles, and allows reuse of unresolved closures without modification. Each particle is assigned a support radius based on its equivalent diameter, using a constant support-radius ratio. Here, a ratio of 3 is adopted, such that the interpolation and spreading domains extend over a radius three times the particle diameter. The main implementation steps are as follows:

1) *Neighboring cell linking*: Each fluid cell is linked to itself and a set of neighboring cells, and each of the connected cells is assigned a weight. This weight is calculated as the product of the kernel function and cell volume and averaged over itself and all neighboring cells.

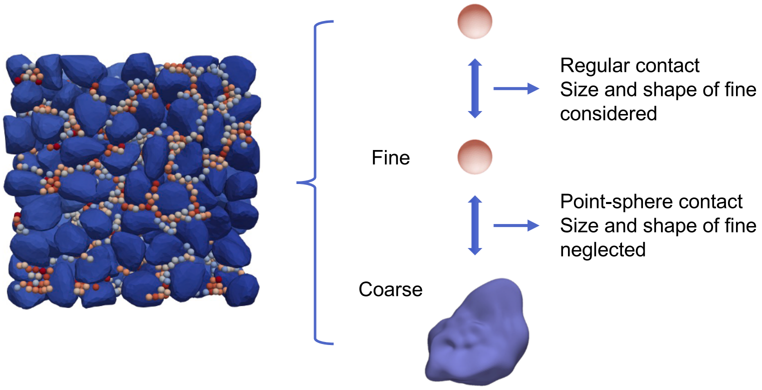

Fig. 5. Illustration of regular and point-sphere contact between a fine sphere and a coarse irregular particle.

2) *Particle-fluid cell association*: Each particle is assigned to a master fluid cell if its centroid falls within that cell. The solid volume of the particle is then distributed among all cells linked to the master cell, and the porosity of each fluid cell is computed based on this distribution.
3) *Fluid property calculation*: The fluid properties (such as velocity, viscosity, and density) of the master fluid cell of a particle are determined by averaging the properties of the cell and its neighbors using the kernel-weighted method.
4) *Fluid-particle interaction*: The interaction between fluid and particles is computed using conventional drag force models with interpolated properties including fluid velocity, viscosity, porosity, particle size, relative particle-fluid velocity, etc.
5) *Interaction spread*: The calculated fluid-particle interaction is distributed back to the master fluid cell and all neighboring cells using the kernel-weighted method.

3.6. *Coarse-fine particle contact algorithm*

To efficiently model interactions between particles of vastly different sizes in polydisperse granular systems, a coarse-fine contact algorithm is proposed based on a point-sphere abstraction. In this model, fine particles are treated as point-like or spherical entities, while coarse particles retain their full geometric descriptions using an SDF representation. This asymmetrical contact formulation significantly reduces computational complexity while maintaining physical accuracy in simulations involving large numbers of fine particles. It should be noted that while this abstraction offers clear advantages in terms of computational efficiency, it does not explicitly capture the shape irregularity of fine particles. The point-sphere model is most appropriate in cases where the local hydrodynamic or contact response is not strongly dependent on the fine particle shape. When shape effects are expected to play a significant role, fine particles should instead be modeled with resolved or semi-resolved geometries. As illustrated in Fig. 5, two representative cases are shown: in the regular contact case, the size and shape of the fine sphere are explicitly considered, whereas in the point-sphere contact case, the fine particle is idealized as a mass point without geometric extent. Contacts between fine particles are resolved using conventional pairwise contact models.

In the fine-coarse contact formulation, the centroid of the fine particle $\vec{x}_{cf}$ is used to query the SDF of a coarse particle. A contact is detected when the effective overlap

$$d_f = \Phi_A(\vec{x}_{cf}) \tag{30}$$

is positive, as defined in Appendix A. The contact normal is obtained from the potential-based contact normal force, and the contact point is taken as the orthogonal projection of the surface projection point $\vec{x}_{cf} = \Pi_A(\vec{x}_{cf})$ onto the line passing through $\vec{x}_{cf}$ and aligned with the contact normal. The contact normal force follows the distance-potential formulation by evaluating the single-node form of Eq. (A.4), with substitutions $d_i \rightarrow d_f$ and $\vec{x}_{P_i} \rightarrow \vec{x}_{cf}$, along with the tangential force calculated by Eq. (A.5) and the relative displacements and velocity defined in Eqs. (A.6) and (A.7), respectively. In the point limit, the branch vector and rotational inertia of the fine particle are set to zero.

The proposed coarse-fine strategy is well suited for multiscale systems where fine particle shapes can be simplified, but interactions with irregular coarse particles remain critical. By treating fine particles as point masses and retaining detailed geometry for coarse particles, the method balances efficiency and geometric fidelity. Although this work uses SDF to represent coarse particles, the point-sphere scheme is general and can be extended to other representations, such as convex shapes handled by the GJK algorithm [44,76,77]. While GJK is faster, it is limited to convex geometries. In contrast, the SDF-based implementation supports arbitrary shapes and is more suitable for realistic particulate systems. Overall, the point-sphere-based coarse-fine contact approach enables scalable simulation of polydisperse media and serves as a flexible component within hybrid CFD-DEM framework.

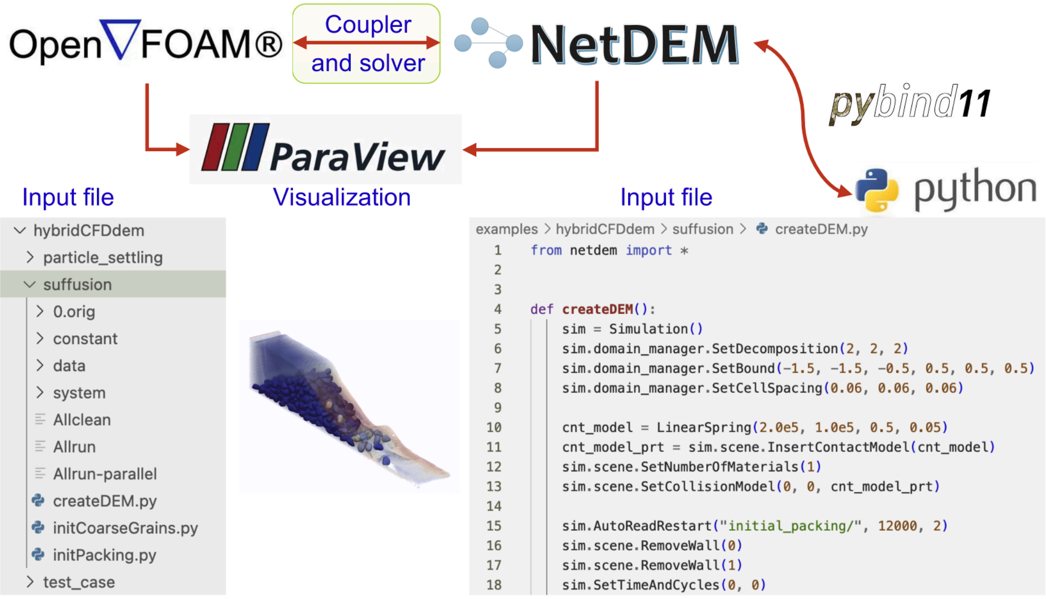

```
hybridCFDdem
  particle_settling
  suffusion
    0.orig
    constant
    data
    system
    Allclean
    Allrun
    Allrun-parallel
    createDEM.py
    initCoarseGrains.py
    initPacking.py
  test_case
```

examples > hybridCFDdem > suffusion > createDEM.py

```python
from netdem import *


def createDEM():
    sim = Simulation()
    sim.domain_manager.SetDecomposition(2, 2, 2)
    sim.domain_manager.SetBound(-1.5, -1.5, -0.5, 0.5, 0.5, 0.5)
    sim.domain_manager.SetCellSpacing(0.06, 0.06, 0.06)

    cnt_model = LinearSpring(2.0e5, 1.0e5, 0.5, 0.05)
    cnt_model_prt = sim.scene.InsertContactModel(cnt_model)
    sim.scene.SetNumberOfMaterials(1)
    sim.scene.SetCollisionModel(0, 0, cnt_model_prt)

    sim.AutoReadRestart("initial_packing/", 12000, 2)
    sim.scene.RemoveWall(0)
    sim.scene.RemoveWall(1)
    sim.SetTimeAndCycles(0, 0)
```

Fig. 6. Illustration of the implementation of the hybrid resolved-unresolved CFD-DEM solver.

4. Implementation, verification and validation

This section presents the implementation of the hybrid CFD-DEM framework and evaluates its fidelity through four benchmark cases: oscillating cylinder in free stream, wedge water entry, single-particle settling, and flow through a packed bed. The first two are classified as validation tests based on comparison with experimental data. The last two serve a dual role: they are verification tests that assess numerical correctness against theoretical or empirical relations, and also validation tests that evaluate the model's capacity to reproduce expected physical behavior. These four tests collectively cover the resolved, semi-resolved, and unresolved regimes and support a comprehensive assessment of model fidelity.

4.1. Implementation

As illustrated in Fig. 6, the hybrid CFD-DEM framework comprises two main components: the CFD solver and the DEM engine. The multiphase CFD algorithms are implemented using OpenFOAM, an open-source platform for solving general fluid dynamics problems [78], while the DEM part is handled by NetDEM, an in-house, machine learning-enabled particle simulation package based on the SDF-DEM framework. OpenFOAM provides a robust infrastructure for modeling multiphase flow, turbulence, and transport phenomena. NetDEM, written in C++, supports arbitrarily shaped particles using SDF representations and enables parallel computation via OpenMP and MPI. A Python interface is built using Pybind11 [79] to facilitate model configuration and runtime interaction. Although neither code was originally designed for coupled simulations, a dedicated hybrid CFD-DEM solver has been developed to integrate the resolved, semi-resolved, and unresolved schemes into a unified framework.

In this implementation, OpenFOAM handles all CFD computations and I/O operations. To enable coupling with the DEM module, a dedicated configuration file `demDict` is introduced, specifying the DEM model through entries `createDEMfile` and `createDEMfunc`. The DEM configuration is typically defined in a Python script, which constructs the particle model and returns it to the solver. Fig. 6 also illustrates a sample script for initializing a DEM simulation and loading a existing pack of particles. While the simulation setup is handled in Python for flexibility, the core DEM computations, particularly contact detection and force evaluation, are implemented in C++ for performance. Particle and contact data can be exported in VTK format during runtime for visualization in ParaView. Regarding interphase momentum exchange in the unresolved regime, the drag closure is configurable and follows the standard OpenFOAM dictionary-based setup. Several commonly used correlations are supported, including the classical Wen-Yu/Ergun-based models, as well as the Di Felice and Koch and Hill type formulations [68,80–82]. In this work, the Gidaspow model is adopted as a representative baseline, as the focus is on the proposed hybrid resolved and unresolved methodology rather than the sensitivity to drag-law selection.

Remark 2. Porosity and VOF treatment: The porosity ϵ represents the fluid-occupiable fraction of a control volume after accounting for the presence of solids, while the VOF phase fraction α denotes the liquid volume fraction within the fluid portion of the cell. In the unresolved scheme, ϵ is computed on a per-cell basis using centroid-based assignment: $\epsilon = 1 - \sum V_p/V_c$, where the summation includes all particle centroids located within the cell. For numerical robustness, ϵ is clipped to the range $[0, 1]$. In the semi-resolved scheme, ϵ is obtained by distributing each particle's volume to a compact stencil of neighboring cells via the interpolation kernel.

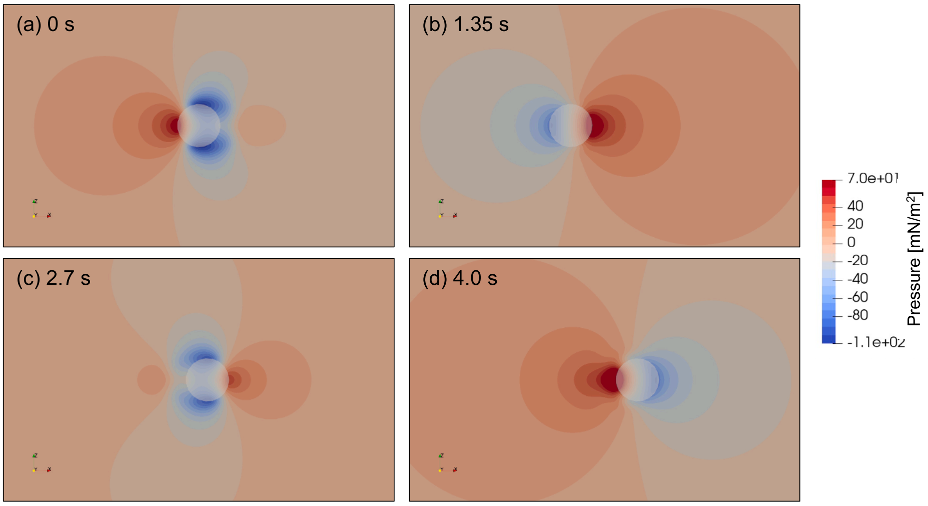

Fig. 7. Pressure contours at different phase angles in the test of oscillating cylinder in a free stream.

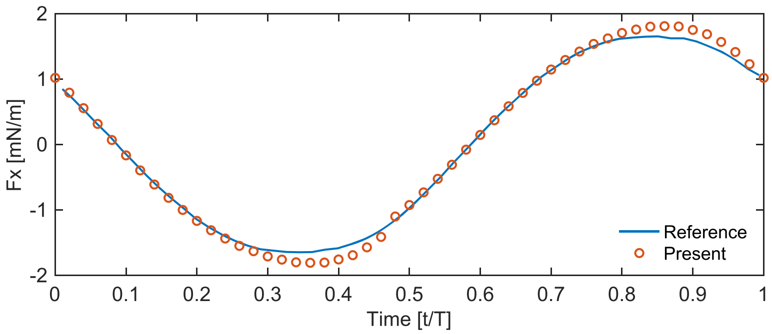

Fig. 8. Evolution of fluid force acting on the cylinder oscillating in a free stream. The reference results are taken from laboratory experiments reported in [84].

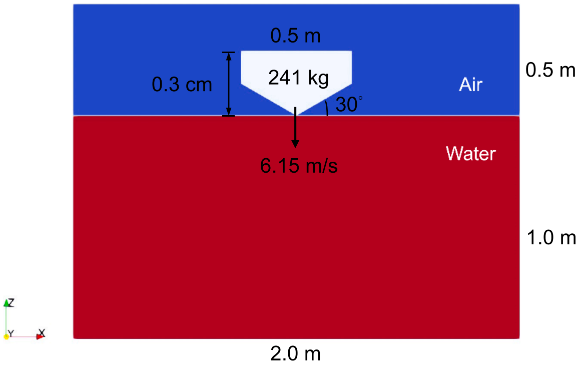

Fig. 9. Model setup of the wedge water entry problem.

The same stencil is used to interpolate porosity back to the particle center for drag evaluation, and to spread the reaction force from particles to the fluid solver (see Eqs. (25)-(27)). In the resolved scheme, coarse solids are not explicitly subtracted from ϵ; instead, their influence is incorporated via the IB source term, which enforces that the local fluid velocity in overlapped cells matches the rigid-body motion. The phase fraction α is advanced using the VOF transport equation (Eq. (5)) with the MULES limiter, which preserves boundedness and maintains a sharp interface. In cells containing both phases ($0 < \alpha < 1$), a single velocity-pressure pair is solved, and material properties in the momentum equation are evaluated using α-weighted mixture rules (Eqs. (3)-(4)). The porosity ϵ enters the governing equations explicitly as the factor representing the fluid-occupiable portion of the control volume, and therefore

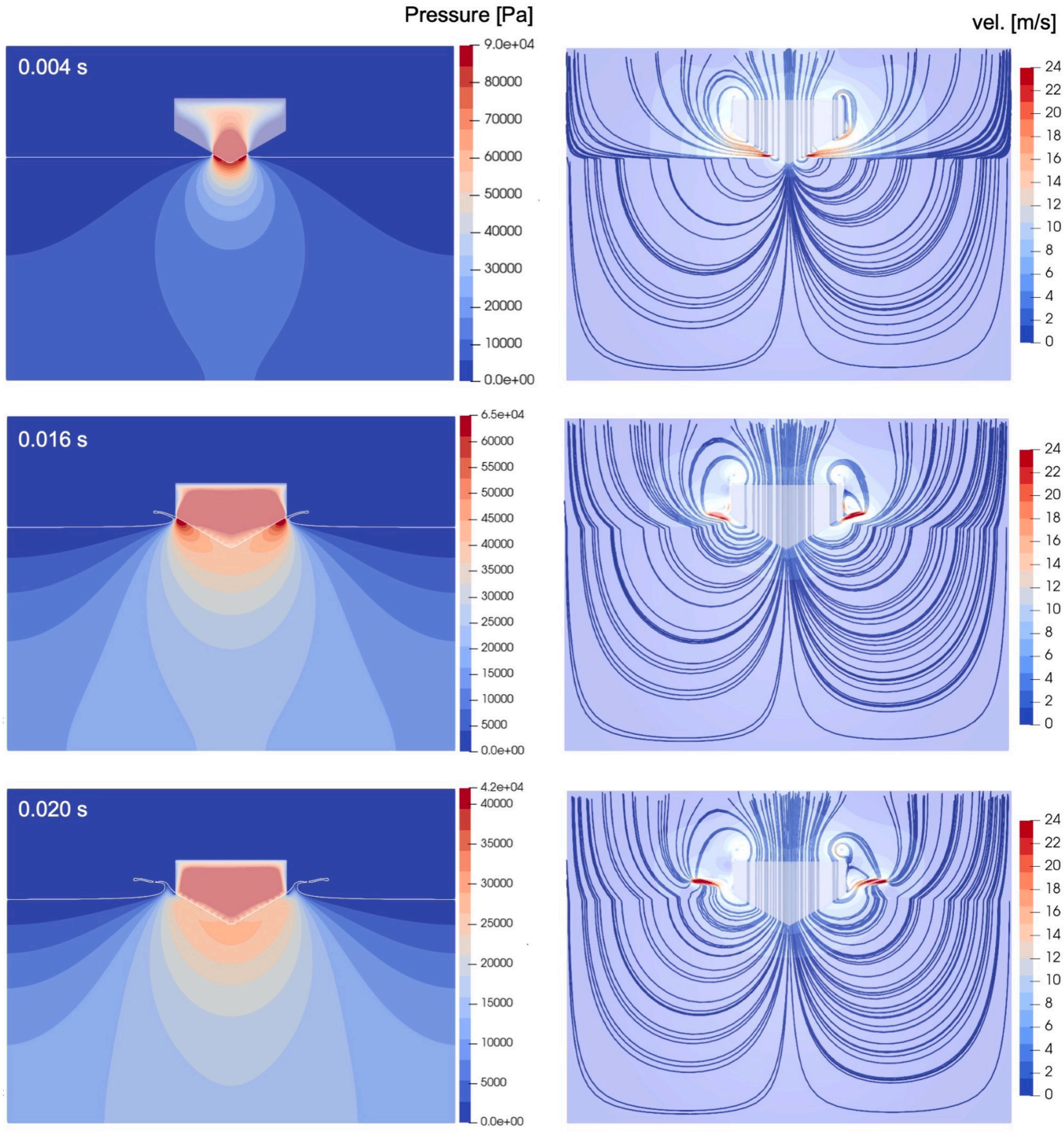

(a) Pressure field (b) Velocity field and streamlines

Fig. 10. Evolution of (a) pressure contours and (b) flow velocity streamlines of the fluid in the wedge water entry problem.

requires no additional correction in interfacial cells. The velocity field $\vec{u}_f$ is treated as the intrinsic (interstitial) velocity, which also sets the relevant Courant scale in porous regions [83].

Remark 3. It is also noted that purely cell-based void-fraction updates may lead to discontinuities in time, as the porosity field changes abruptly when a particle crosses a cell boundary. As a result, the time derivative of porosity becomes undefined in the limit of vanishing timestep. No additional regularization is introduced in the classical unresolved formulation used here, but the semi-resolved treatment alleviates this issue by distributing particle volume smoothly across neighboring cells. This regularization ensures continuity in time and avoids timestep-dependent instabilities.

4.2. Oscillating cylinder in free stream

This test examines the fluid response to a harmonically oscillating cylinder in an initially quiescent fluid, a classical benchmark problem relevant to various engineering applications [61,84]. The setup follows the experimental configuration in [84], where a cylinder of diameter 0.01 m is placed at the center of a fluid domain of width 0.5 m and height 0.3 m. The cylinder undergoes prescribed horizontal oscillation given by $x(t) = -A\sin(2\pi f t)$, with amplitude $A = 0.008$ m and frequency $f = 0.2$ s^{-1}. The fluid is

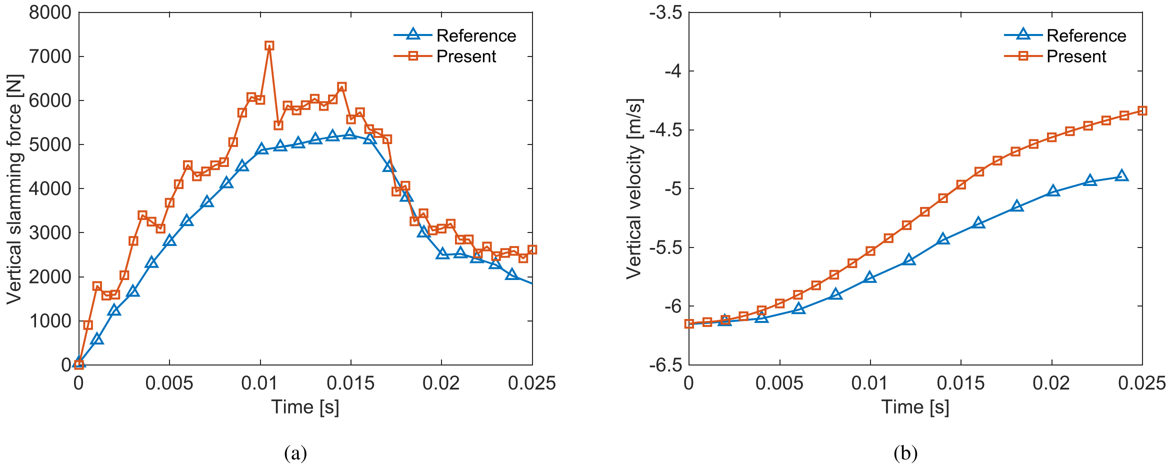

Fig. 11. Evolution of (a) vertical slamming force and (b) vertical velocity of the wedge in the wedge water entry problem. The reference results are taken from experiments reported in [85,86]. Note that the slamming force is measured for only 0.2 m of the wedge length.

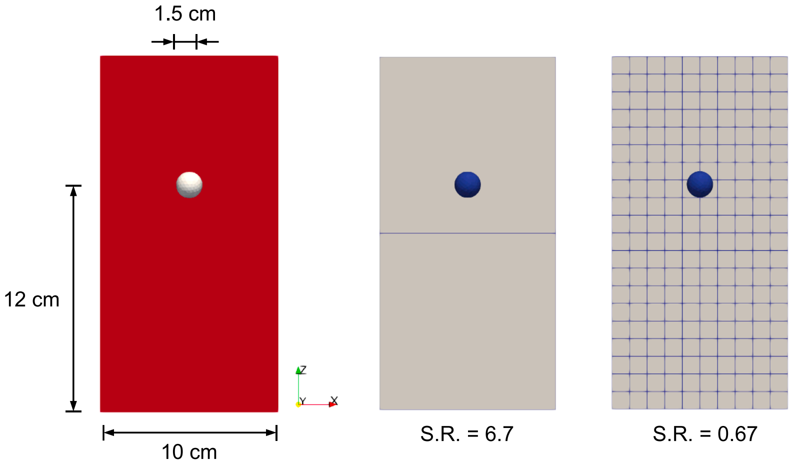

Fig. 12. Model setup for the single particle settling test, together with two example meshes. S.R., abbreviation of size ratio, represents the ratio of mesh size to particle size.

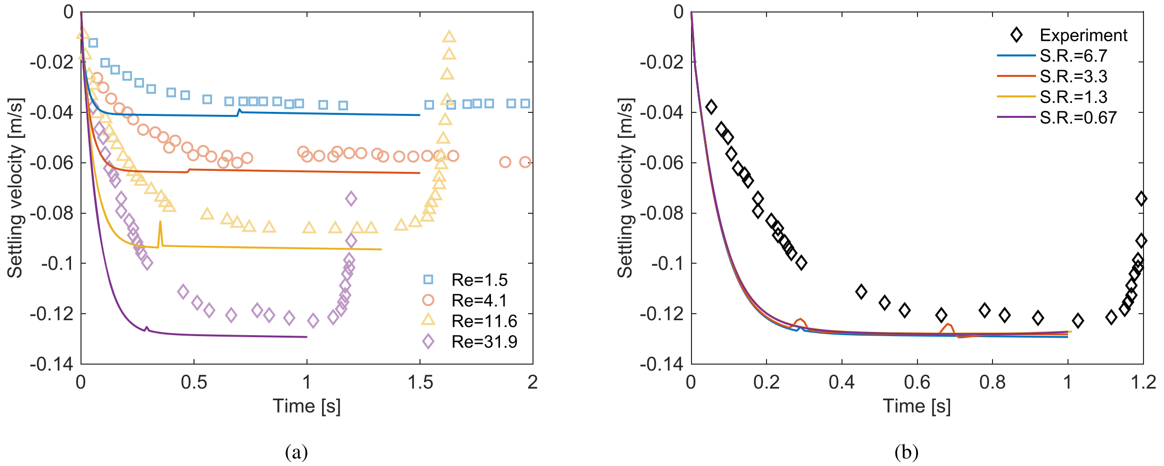

Fig. 13. Evolution of the settling velocity of spherical particles for the cases of different fluid densities and viscosity: (a) unresolved case with mesh size 0.01 m, and (b) semi-resolved case with different mesh sizes. The markers indicate the results of laboratory experiments from [87], and the lines represent the results of hybrid CFD-DEM simulations.

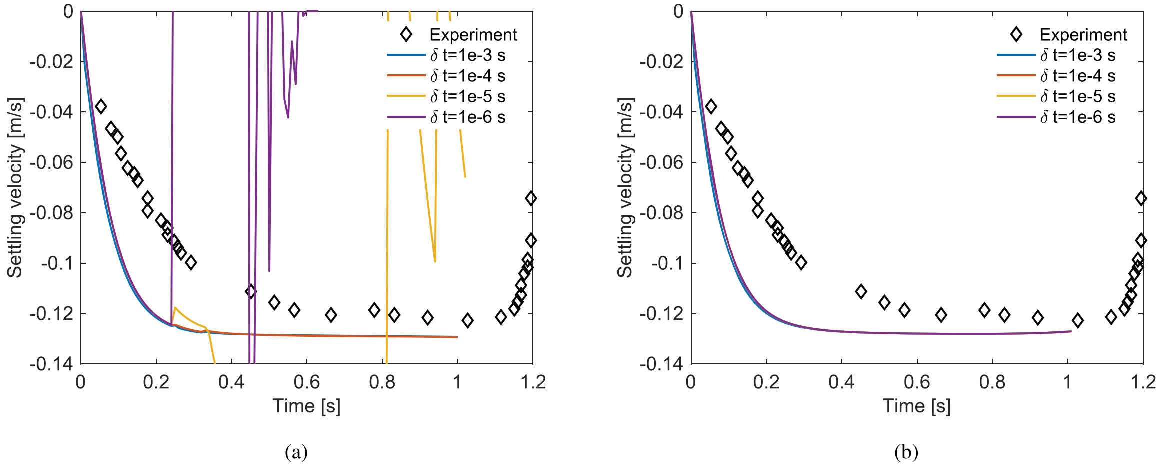

Fig. 14. Timestep refinement for the single-particle settling test: (a) S.R. = 6.7 (cell-local void-fraction update), and (b) S.R. = 0.67 (semi-resolved filter distributing particle volume over neighboring cells). Each panel compares CFD timesteps of 10^{-3} s, 10^{-4} s, 10^{-5} s, and 10^{-6} s.

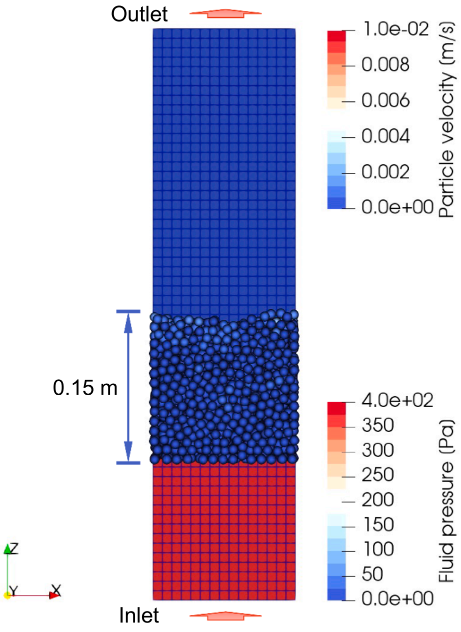

Fig. 15. Model setup for the Ergun's packed bed test.

water, with density $\rho = 1000$ kg/m^3 and dynamic viscosity $\mu = 0.001$ Ns/m^2. The simulation is performed in two dimensions, using a uniform grid of 1000×600 cells. The timestep in CFD is set adaptively based on local Courant number constraints. Fig. 7 shows the pressure contours at different phase angles during the oscillation cycle. Fig. 8 presents the time history of the fluid force acting on the cylinder. The results are in good agreement with both experimental data and prior numerical studies [61,84], validating the resolved fluid-structure coupling within the proposed framework.

4.3. Water entry of wedge

The entry of a wedge into water is a typical problem that involves two-phase fluid and an irregular-shaped solid body, where laboratory experiments can been found in Zhao et al. [85]. As illustrated in Fig. 9, for this verification test, the fluid domain has a width of 2.0 m and a height of 1.5 m, and the water depth is 1.0 m. The density and viscosity of the water is 1000 kg/m^3 and 0.001 Ns/m^2, respectively; and the density and viscosity of the air is 1.2 kg/m^3 and 1.75×10^{-5} Ns/m^2, respectively. The surface tension between water and air is 0.07 N/m. The whole wedge consists two parts, namely a triangular-prism drop rig with a deadrise angle of 30° and a rectangular-prism blast. The breadth of the wedge is 0.5 m, the height is 0.29 m, and the total weight is 241 kg. For simplicity, the problem is modeled in two-dimension with a mesh of 500 by 375 elements for the fluid. The wedge is modeled as

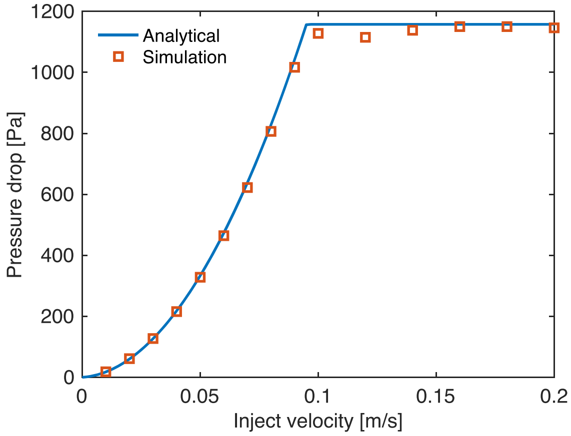

Fig. 16. Pressure drop versus inlet velocity in the Ergun’s test. Analytical reference based on Eq. (31).

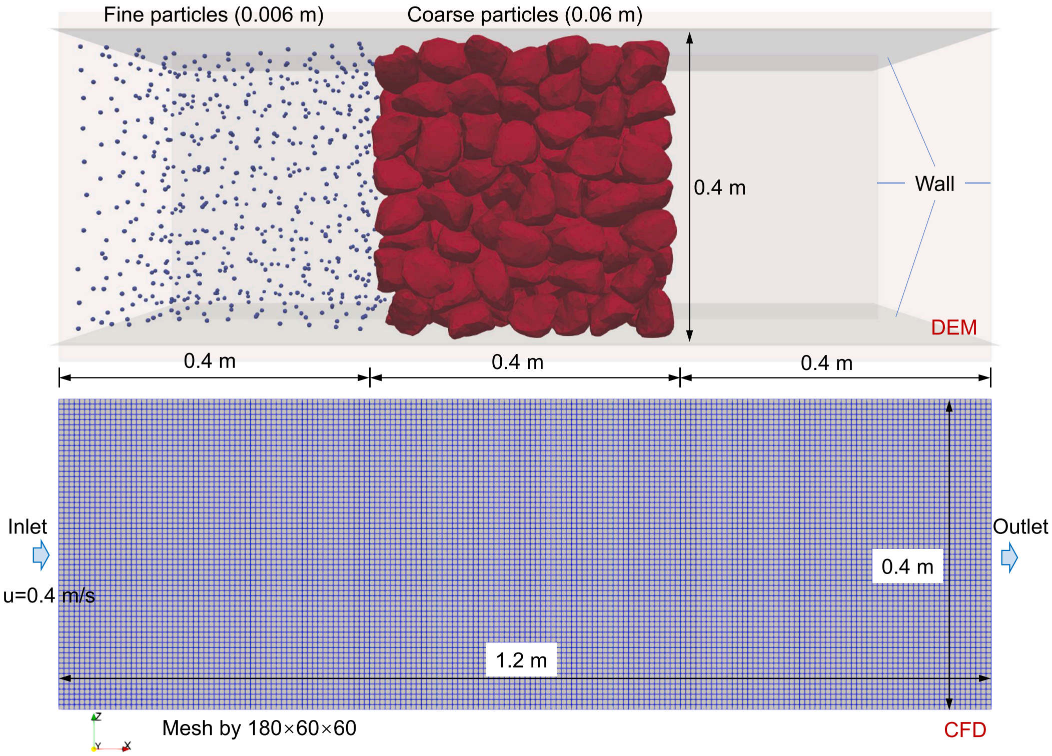

Fig. 17. Model setup for the filtration of fine particles through coarse granular media.

polyhedron in the simulation. It is released from a certain height above the water and when it touches the water surface, the wedge would develop a vertical velocity of -6.15 m/s.

Fig. 10 illustrates the evolution of fluid pressure contours during wedge water entry. As the wedge penetrates the water surface, an initial splash forms along its boundaries, followed by flow detachment as entry continues. Elevated pressure regions originate at the keel and propagate downward into the fluid domain. The simulated pressure distribution shows good agreement with the results reported by [86]. For quantitative evaluation, Fig. 11 presents the time history of vertical slamming force and vertical velocity of the wedge. A sharp rise in slamming force is observed within the first 0.015 s, followed by a gradual transition to a quasi-steady regime. Correspondingly, the vertical velocity decreases rapidly before approaching a slower descent rate. Compared to experimental data [85,86], the simulation slightly overpredicts the peak slamming force and underpredicts the velocity, potentially due to the absence of three-dimensional effects in the two-dimensional modeling framework. It is noted that although the hybrid CFD-DEM solver is employed, this case degenerates to a fully resolved configuration, wherein the wedge is explicitly represented with a signed distance

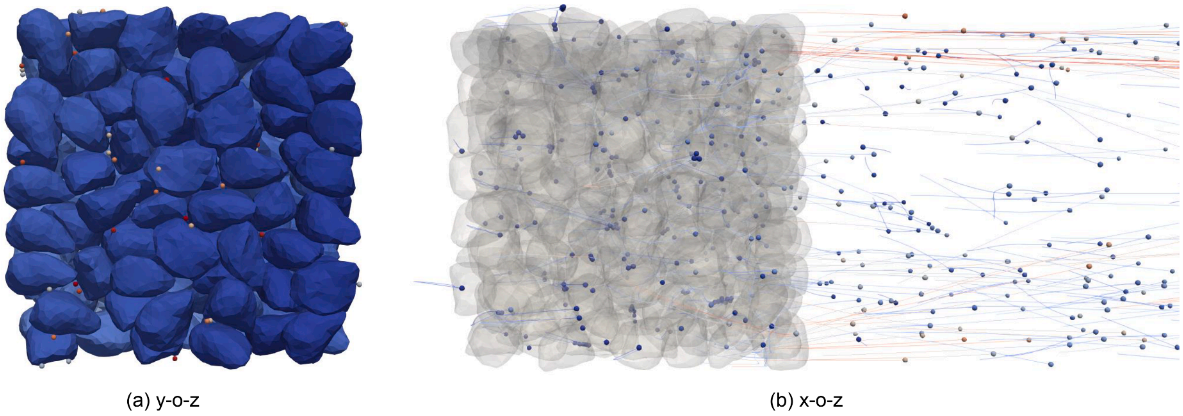

Fig. 18. Snapshots of the coarse and fine particles at the end of the filtration simulation: (a) y-o-z plane view and (b) x-o-z plane view.

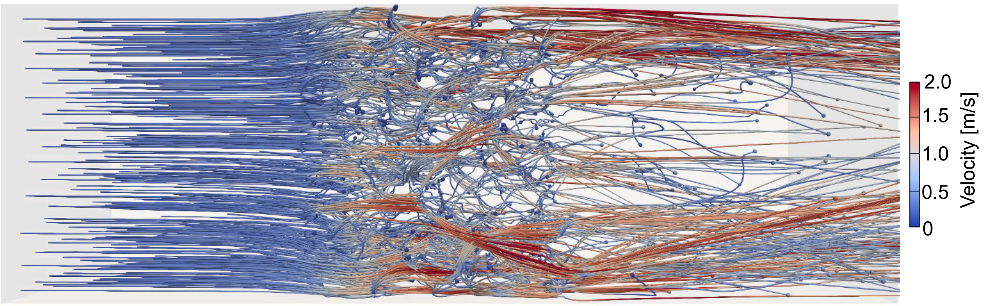

Fig. 19. Trajectories of fine particles during the filtration process.

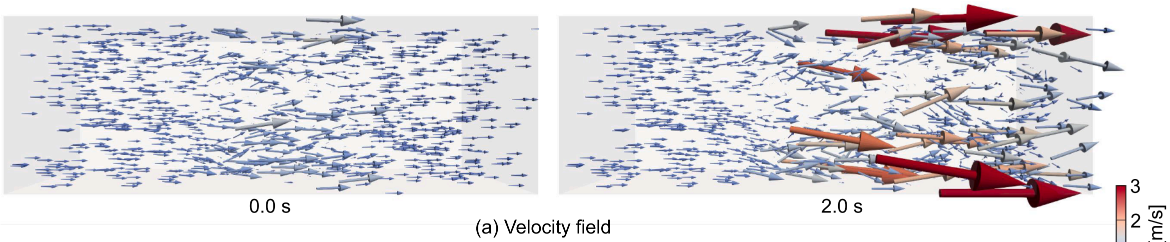

(a) Velocity field

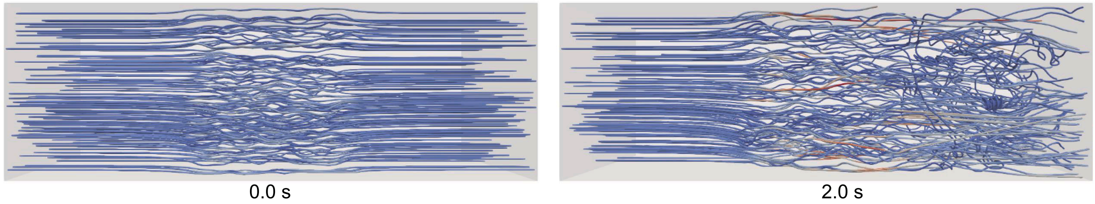

(b) Streamlines

Fig. 20. Fluid velocity field (a) and streamlines (b) of the filtration test.

field. The reasonable agreement with benchmark data further confirms the accuracy and robustness of the resolved mode within the proposed hybrid framework.

4.4. Single-particle settling test

The settling behavior of a single particle is investigated to validate both the unresolved and semi-resolved coupling strategies of the proposed hybrid CFD-DEM framework. Numerical results are compared with the well-documented laboratory experiments reported by ten Cate et al. [87]. As illustrated in Fig. 12, a spherical particle with a diameter of 1.5 cm and a density of $1120\,\mathrm{kg/m^3}$

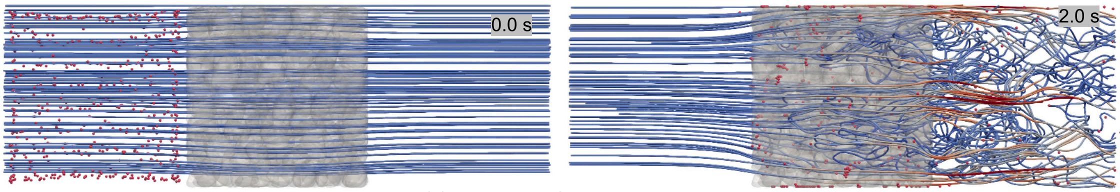

(a) Unresolved CFD-DEM model

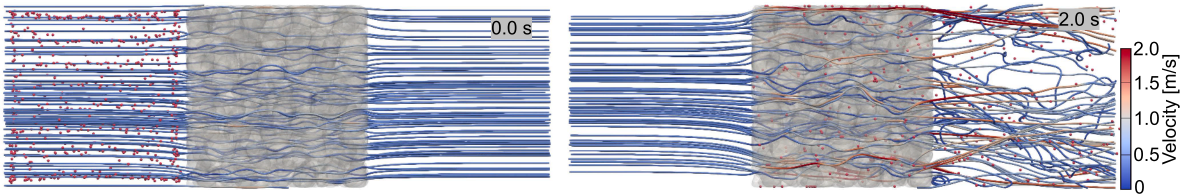

(b) Hybrid resolved CFD-DEM model

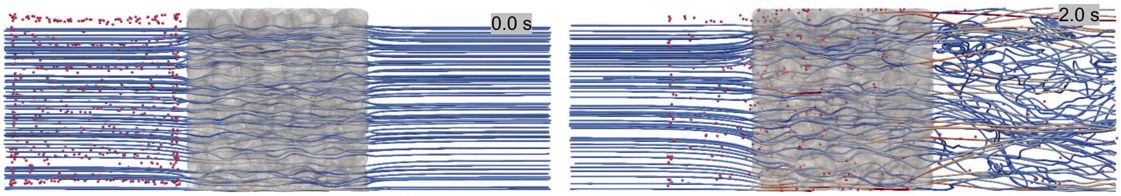

(c) Resolved CFD-DEM model

Fig. 21. Streamlines and fine particles trajectories simulated based on (a) the single unresolved approach, (b) hybrid resolved-unresolved approach, and (c) the single resolved approach.

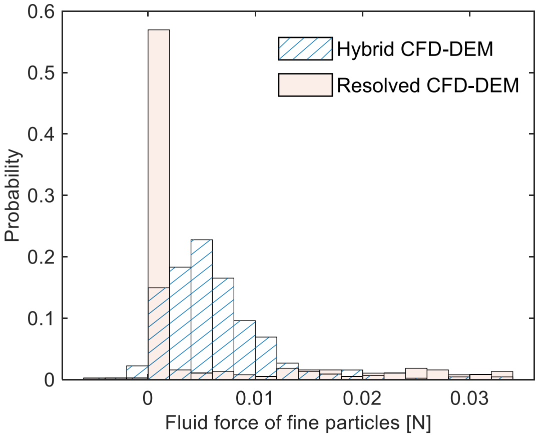

Fig. 22. Comparison of the x-component of fluid-particle interaction force of the fine particles within the coarse grains simulated based on different approaches.

is initially positioned 12 cm above the bottom of a square container with a cross-sectional area of 10 cm by 10 cm. The surrounding fluid properties, including density and dynamic viscosity, are adopted directly from the experimental configurations reported in [87]. Four different CFD mesh resolutions are considered, with cell sizes of 10 cm, 5 cm, 2 cm, and 1 cm, corresponding to mesh-to-particle size ratios of 6.7, 3.3, 1.3, and 0.67, respectively. These cases span both unresolved and semi-resolved regimes. The CFD and DEM timesteps are set to 10^{-3} s and 10^{-7} s, respectively, unless otherwise specified.

Fig. 13 presents comparisons between the simulated settling velocity histories and the corresponding experimental measurements under different fluid conditions. Overall, the predicted terminal velocities exhibit good agreement with experimental data, with deviations within 10%, as summarized in Table 1 . This level of agreement indicates that the drag formulations employed in both unresolved and semi-resolved schemes are capable of capturing steady-state settling behavior under appropriate conditions. In the unresolved case, simulations remain stable when the CFD cell size is much larger than the particle diameter. However, as the mesh is refined and the cell size approaches the particle size, the accuracy of cell-based porosity evaluations deteriorates, leading to numerical instabilities. In contrast, the semi-resolved scheme maintains stability and consistency across all tested mesh resolutions, owing to its smooth volume distribution strategy that ensures well-behaved porosity fields and robust fluid-particle coupling.

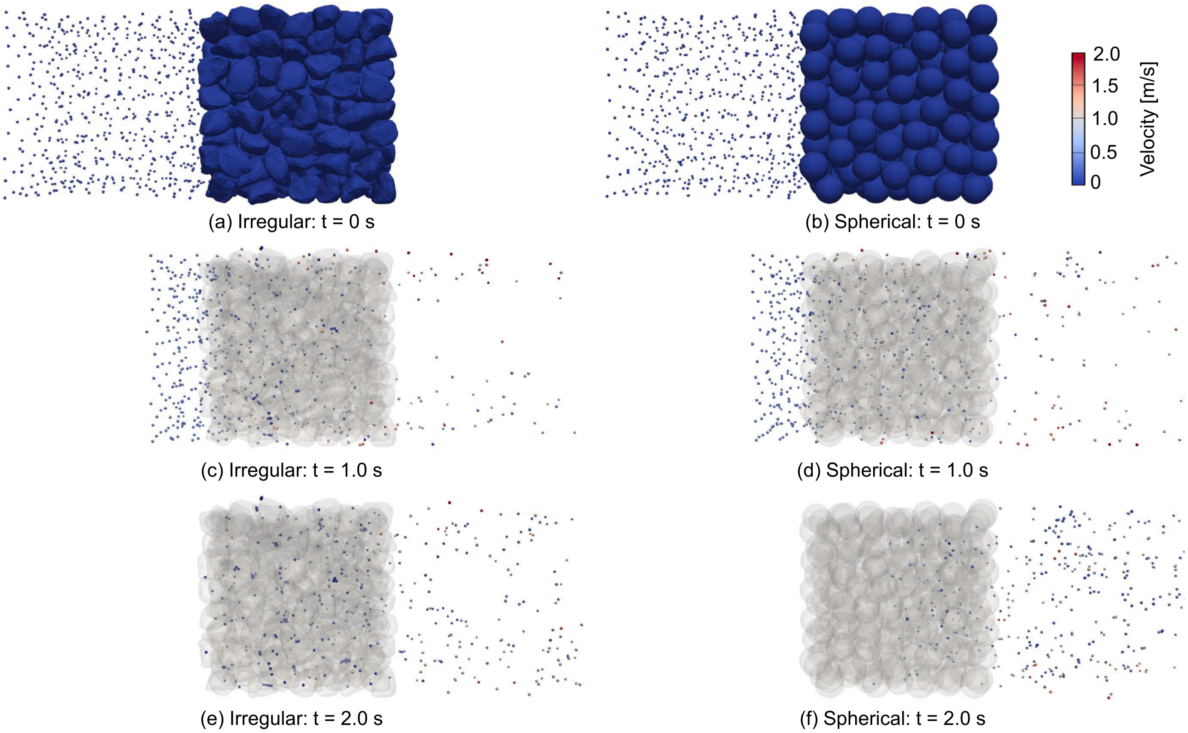

Fig. 23. Snapshots of the filtration process for the cases of different shapes of coarse grains. Left column: irregularly-shaped case; right column: spherical case.

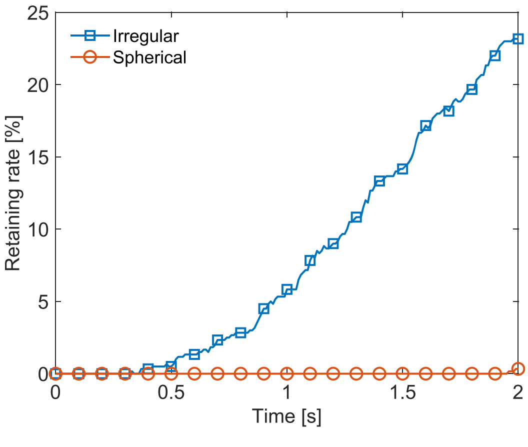

Fig. 24. Retaining ratio over time for different shapes of coarse grains.

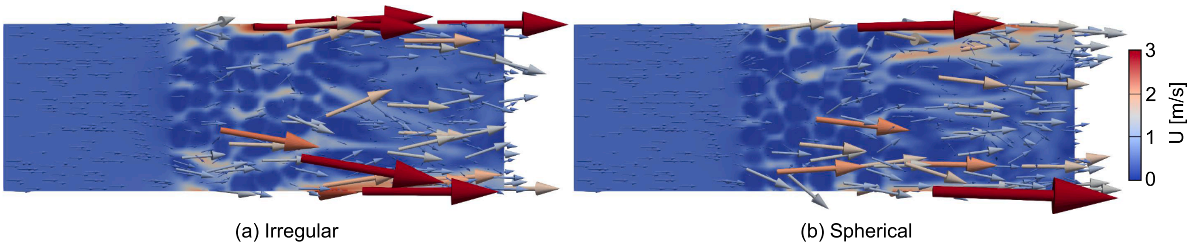

Fig. 25. Fluid velocity field for different shapes of coarse grains: (a) irregularly-shaped case and (b) spherical case.

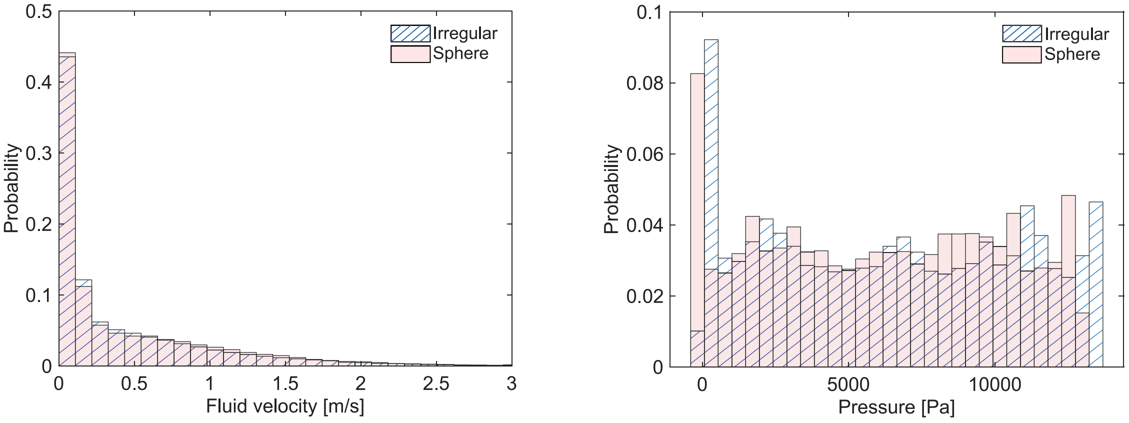

(a) (b)

Fig. 26. Probability density functions of (a) fluid velocity and (b) fluid pressure within the coarse particle region for spherical and irregular particle configurations. The irregular case exhibits a broader pressure distribution, reflecting stronger flow resistance.

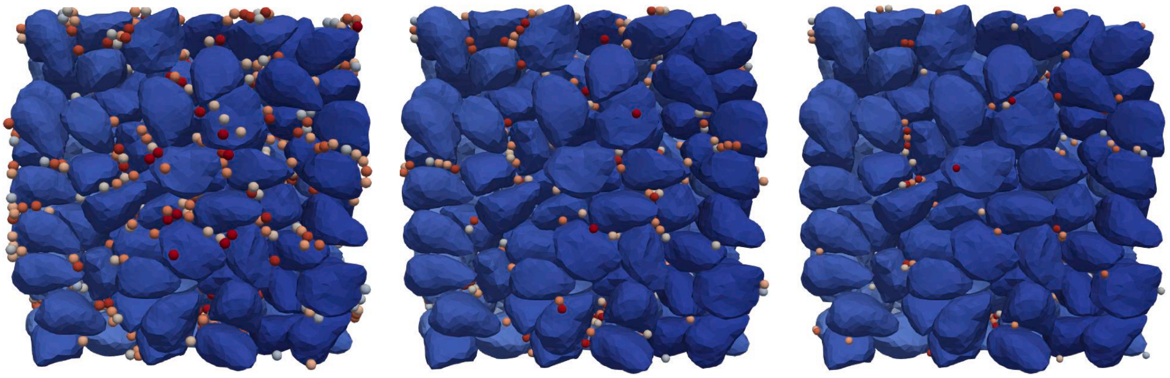

(a) Size ratio = 5 (b) Size ratio = 6 (c) Size ratio = 7

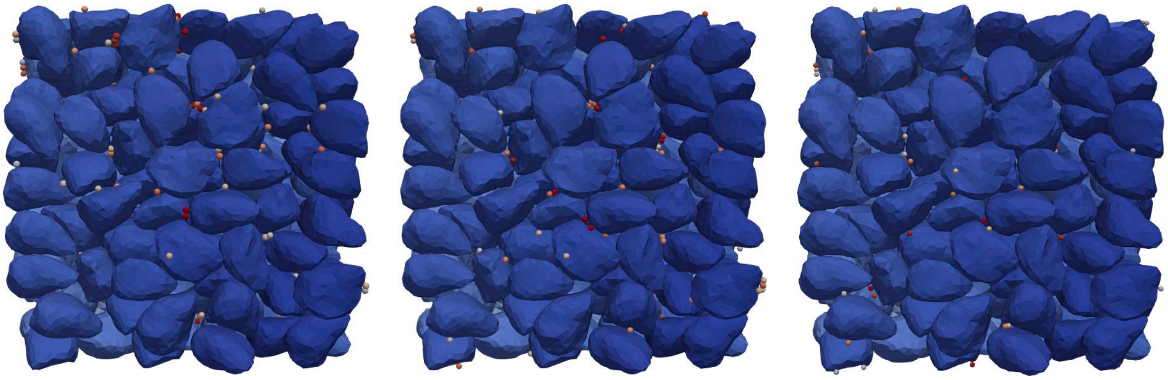

(d) Size ratio = 8 (e) Size ratio = 9 (f) Size ratio = 10

Fig. 27. Snapshots of coarse and fine particles at the end of the filtration simulation for different coarse to fine particle size ratios.

Transient discrepancies are observed in both the unresolved and semi-resolved cases, particularly during the initial acceleration phase. These deviations can be attributed to two primary factors. First, the present implementation has not considered the effects of added mass and history force, which are known to influence the early-time dynamics of particles accelerating in a fluid [88]. The absence of these contributions leads to a moderate overprediction of velocity during the transient stage, although their influence diminishes once steady-state conditions are reached. Second, in unresolved cases, localized velocity overshoots arise when particles cross CFD cell boundaries. These overshoots originate from abrupt changes in the cell-based porosity field, which induce discontinu-

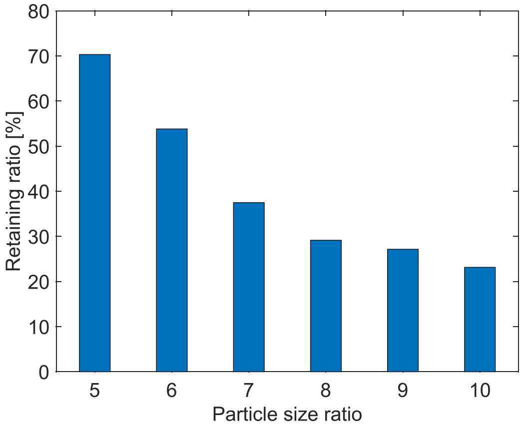

Fig. 28. Retaining ratio at the end of the filtration simulation for different particle size ratios.

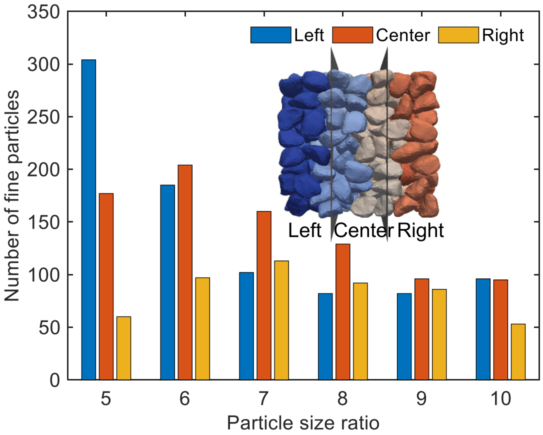

Fig. 29. Distribution of fine particles at the end of the filtration simulation for different particle size ratios.

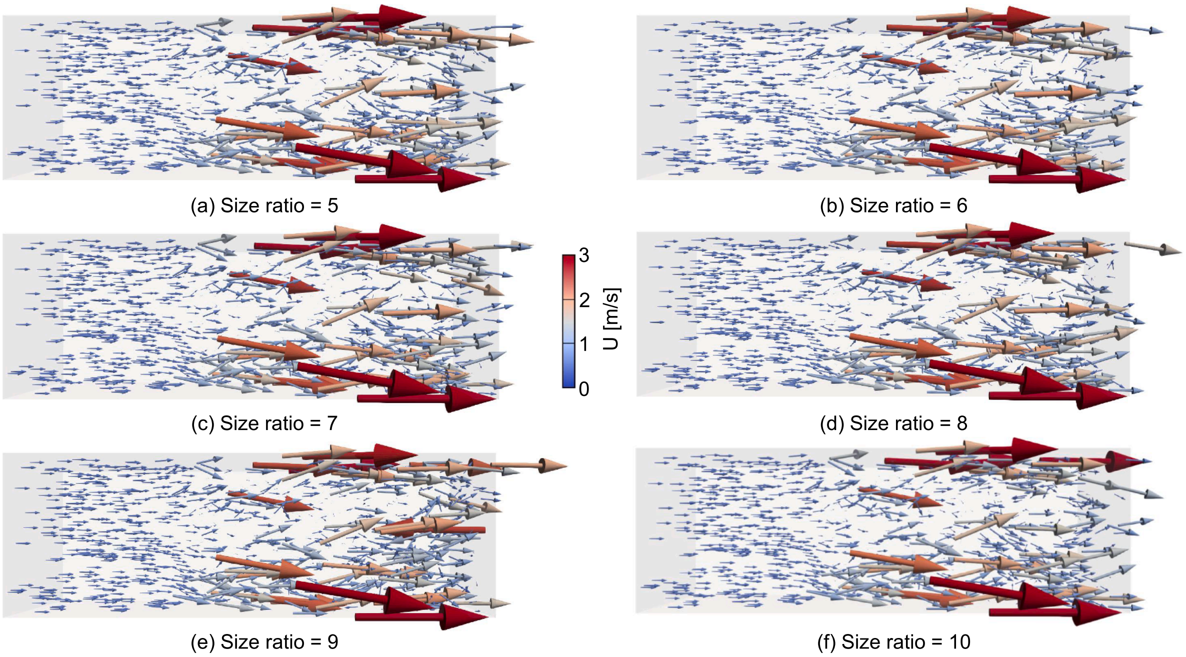

Fig. 30. Fluid velocity field for different particle size ratios between the coarse to the fine.

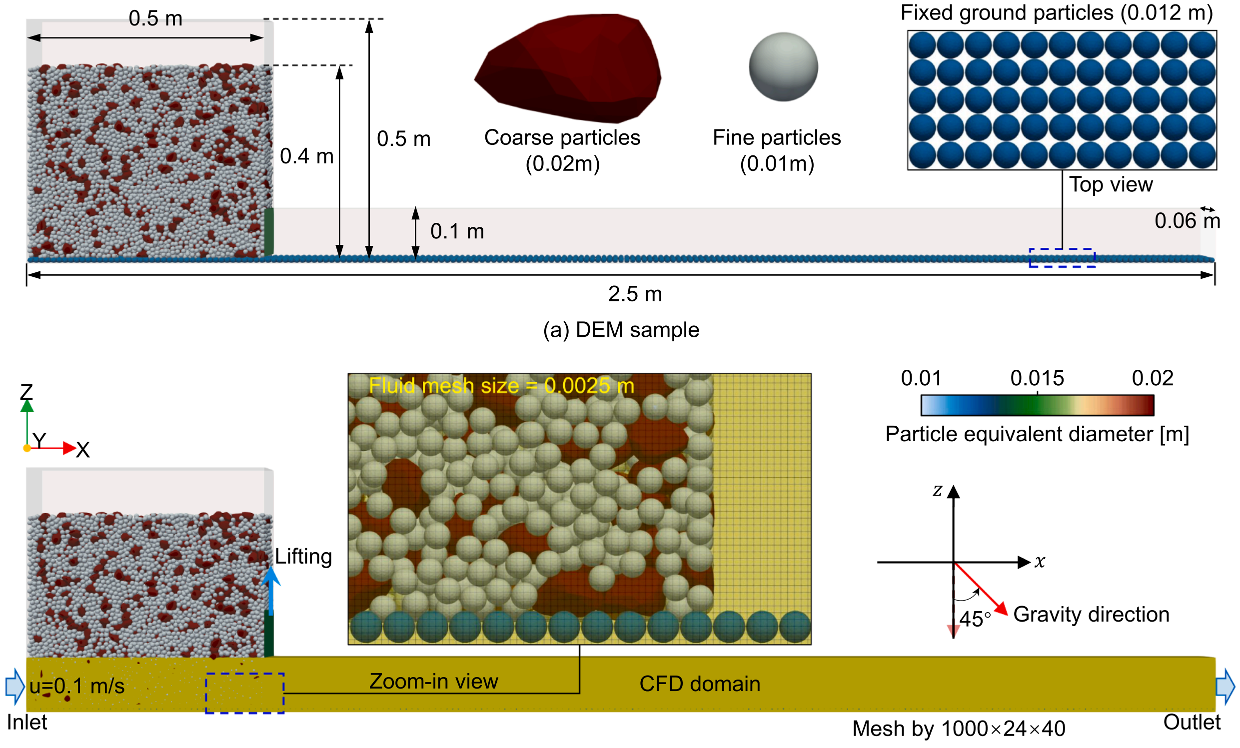

(a) DEM sample

(b) CFD-DEM model

Fig. 31. Model setup for simulating particle sorting in a fluid-driven granular chute flow.

Table 1
Specifications and results of the spherical particle settling tests. Here, v_∞ denotes the steady-state settling velocity; exp., sim., and eqn. refer to experimental data, simulation results, and predictions from Eqs. (17)–(19), respectively. The experimental results are taken from [87].

Case number	ρ_f [kg/m^3]	μ_f [$\times 10^{-3}$ Ns/m^2]	v_∞, exp. [m/s]	v_∞, sim. [m/s]	v_∞, eqn. [m/s]
Case 1	970	373	0.038	0.041	0.041
Case 2	965	212	0.060	0.064	0.064
Case 3	962	113	0.086	0.094	0.094
Case 4	960	58	0.123	0.129	0.129

ities in the evaluated fluid-particle interaction forces. Such behavior is a known artifact of Eulerian-Lagrangian coupling approaches relying on cell-local porosity definitions. The magnitude of these overshoots depends on the relative particle position during cell crossing; for instance, the pronounced fluctuation observed in the case with $Re = 11.6$ corresponds to such an event. These artifacts are progressively alleviated as the mesh is refined and a semi-resolved formulation is adopted, in which the particle volume is smoothly distributed over multiple neighboring cells.

To further examine the influence of timestep size on porosity evolution, a timestep refinement study is conducted for two representative size ratios. The first case corresponds to S.R. = 6.7, where the particle is effectively confined within a single fluid cell and the porosity is evaluated using a cell-local mapping. The second case considers S.R. = 0.67, for which the particle volume is distributed across multiple cells via the semi-resolved filtering approach. For both cases, the CFD timestep is varied from 10^{-3} s to 10^{-6} s, while the DEM timestep is kept constant. The corresponding results are presented in Fig. 14. In the unresolved configuration (S.R. = 6.7), the simulation becomes unstable when the timestep is reduced to 10^{-5} s or smaller, as the discrete porosity jumps induced by particle-cell crossings lead to numerical divergence. This behavior reflects a fundamental limitation of cell-based porosity updates, in which the temporal derivative of porosity becomes ill-defined as the timestep approaches zero. In contrast, the semi-resolved case (S.R. = 0.67) remains stable across all tested timesteps and exhibits nearly identical velocity histories. This robustness arises from the smooth spatial filtering of particle volume, which effectively regularizes the temporal evolution of porosity. These results demonstrate that the semi-resolved formulation not only improves spatial accuracy but also significantly enhances numerical stability with respect to timestep refinement.

(a) t = 0.0 s

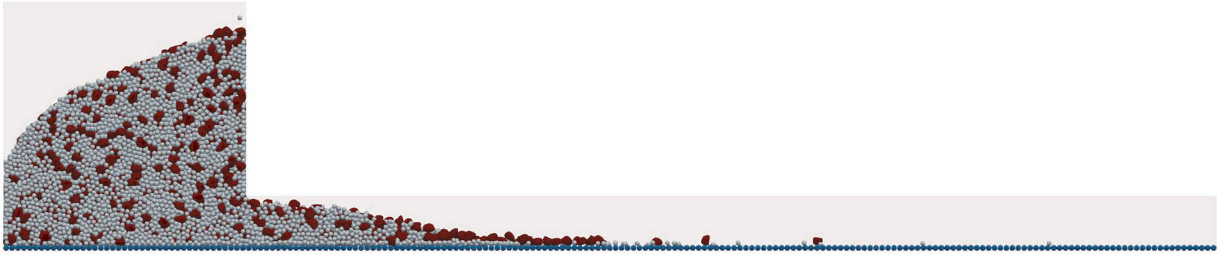

(b) t = 2.5 s

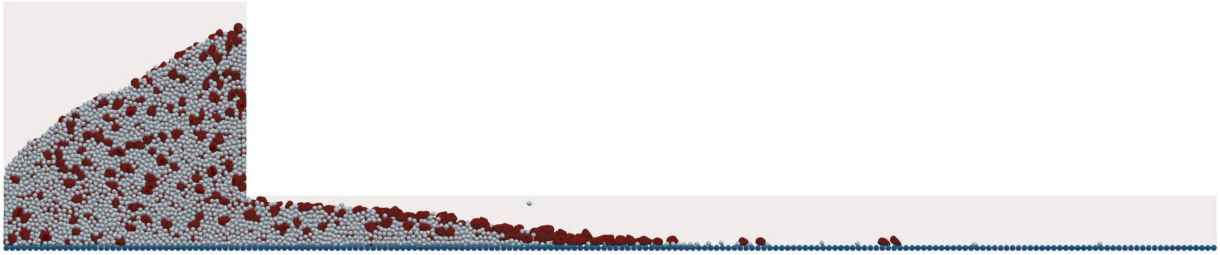

(c) t = 5.0 s

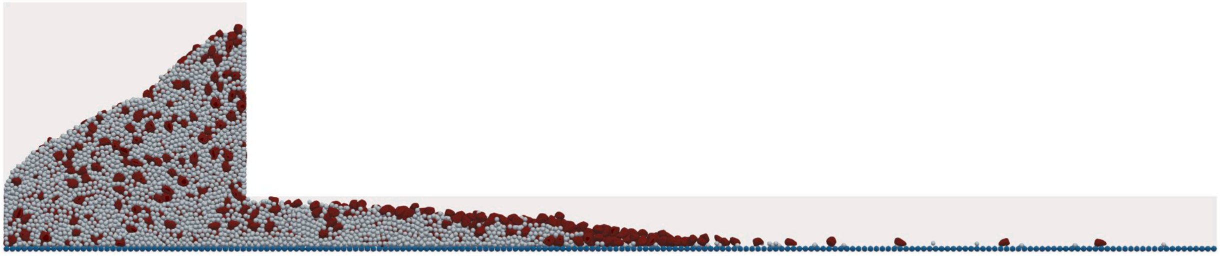

(d) t = 7.5 s

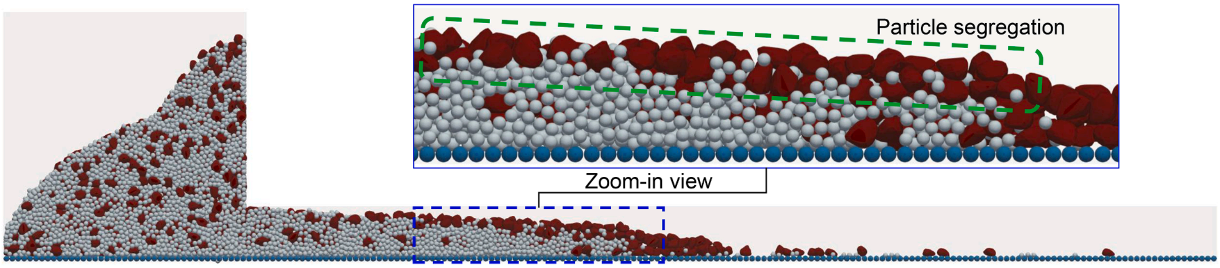

(e) t = 10 s

Fig. 32. Snapshots showing the evolution of particle size sorting over time during channelized transport.

4.5. Ergun's packed bed test

This test simulates upward flow through a packed particle bed to validate the semi-resolved CFD-DEM formulation against the classical Ergun equation [70]. Approximately 3400 particles of diameter 0.01 m are placed in a cubic container with a base of 0.15 m by 0.15 m, reaching a packing height of approximately 0.15 m. The surrounding fluid domain has the same cross-section and extends to a total height of 0.6 m, with the packed bed located between 0.15 m and 0.3 m. The bottom boundary imposes a fixed inlet velocity,

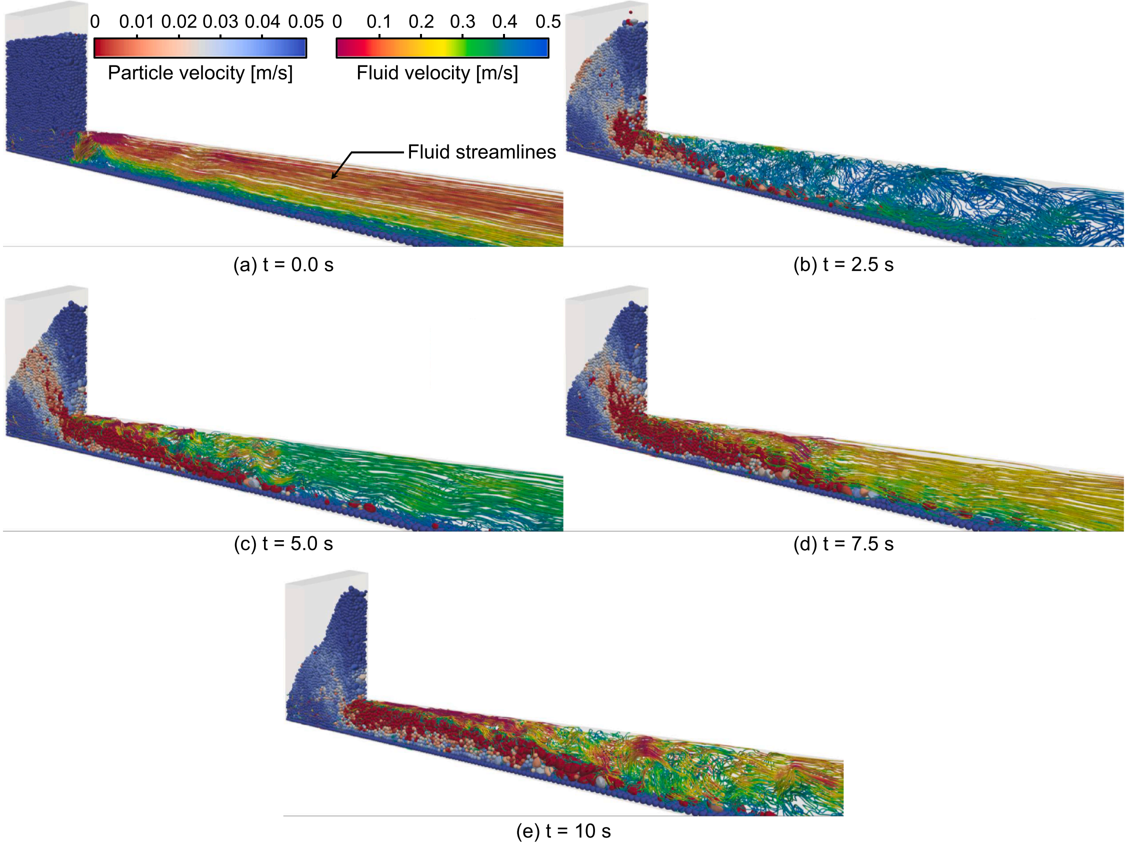

(a) t = 0.0 s (b) t = 2.5 s

(c) t = 5.0 s (d) t = 7.5 s

(e) t = 10 s

Fig. 33. Evolution of particle velocities and fluid streamlines during the sorting process.

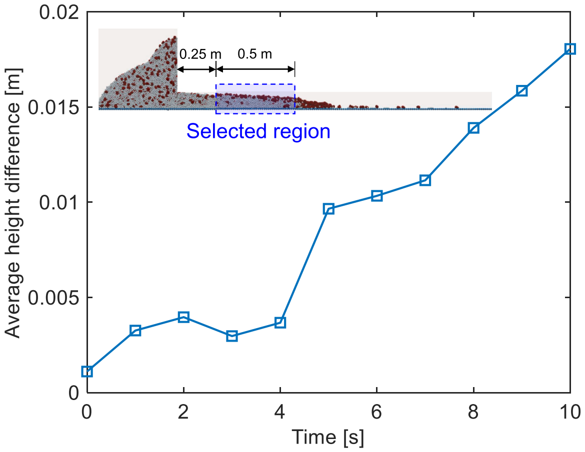

Fig. 34. Temporal evolution of the average height difference between coarse and fine particles within the run-out front region. The increasing separation over time reflects the development of inverse grading during the flow.

while the top is set as a pressure outlet. Inlet velocities are varied to span both the fixed-bed and fluidization regimes. The fluid is water, and the CFD mesh size is equal to the particle diameter (0.01 m), placing this case in the semi-resolved regime. The DEM adopts a linear contact model with normal stiffness of 2.0×10^6 N/m, shear stiffness of 1.0×10^6 N/m, contact friction of 0.3, and numerical damping of 0.3. To avoid wall-induced shear resistance during fluidization, the particle-wall contact friction is set to zero. Fig. 15 illustrates the simulation setup.

The pressure drop across the particle bed is computed for different inlet velocities and compared to the analytical prediction as [70]:

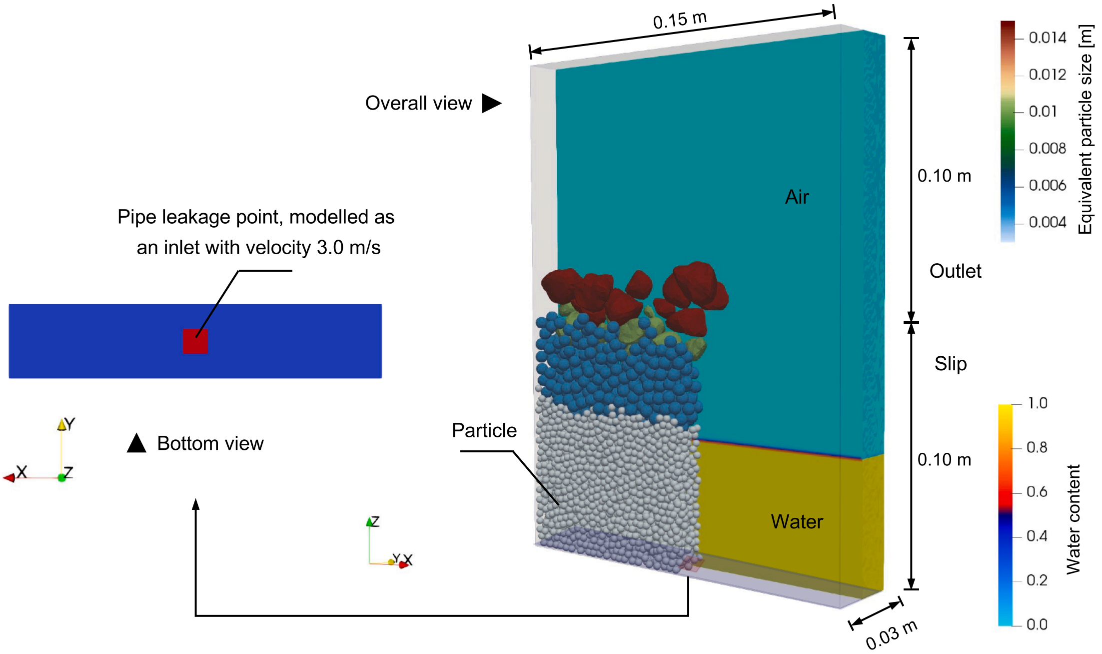

Fig. 35. Model setup for simulating the jet-induced destabilization in granular media. The fluid and particle domains are visualized using half-section views along the *y*- and *x*-axes, respectively.

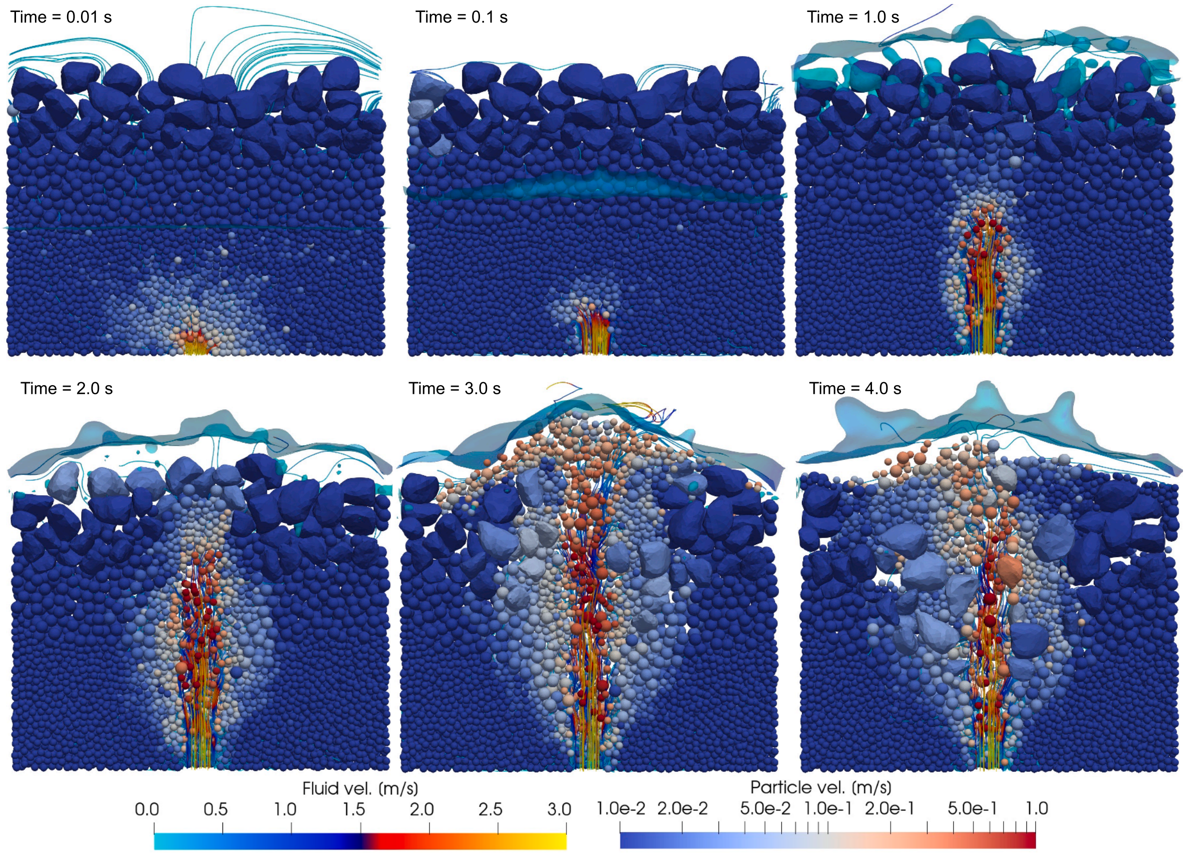

Fig. 36. Snapshots of jet-induced particle mobilization and surface evolution at representative times.

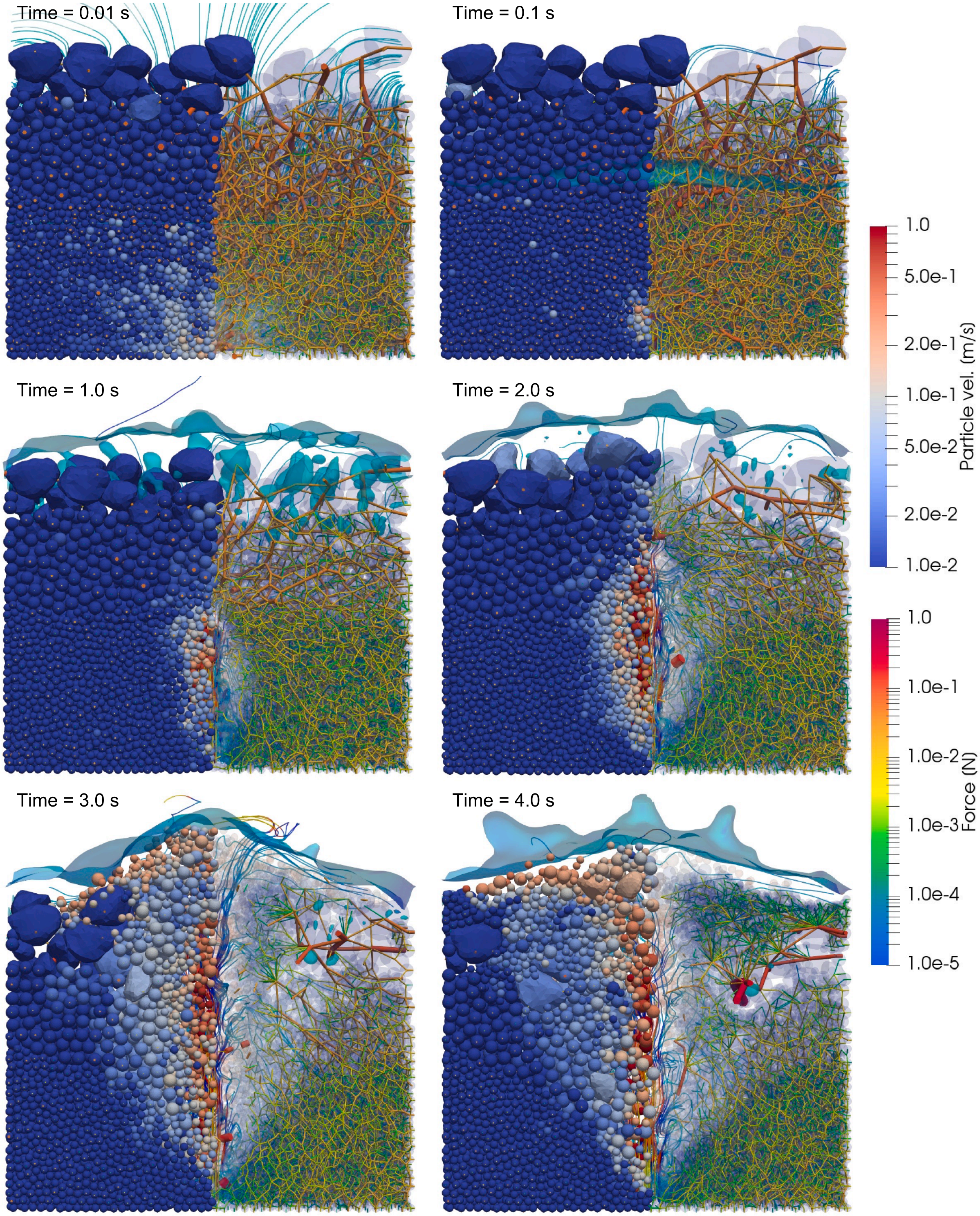

Fig. 37. Evolution of force chain and internal failure during the process of jet-induced destabilization in granular media.

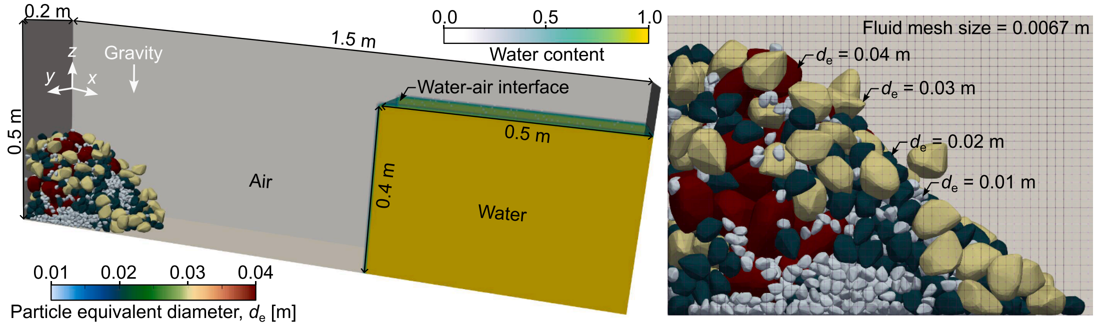

(a) Model set-ups: geometry and initial sample

(b) Size comparison: particle vs. fluid mesh

Fig. 38. Model setup for simulating the dam-break flow impacting a granular bed.

Table 2
Model parameters of the flirtation example.

Domain	Properties	Values
CFD	Domain size	1.2 m × 0.4 m × 0.4 m
	Discretization	180 × 60 × 60 cells
	Density	1000 kg/m^3
	Viscosity	1.0e-6 m^2/s
	Timestep	adaptive
DEM	Number of coarse & fine particles	384, 600
	Particle size	0.06, 0.006 m
	Particle density	2600 kg/m^3
	Contact normal & tangential stiffness	2.0e5, 1.0e5 N/m
	Contact friction coefficient	0.5
	Contact damping coefficient	0.05
	Timestep	1.0e-4 s

$$\frac{\Delta p}{\Delta h} = 150\frac{(1-\epsilon)^2}{\epsilon^3}\frac{\mu_f \vec{u}_f}{d^2} + 1.75\frac{(1-\epsilon)}{\epsilon^3}\frac{\rho_f \vec{u}_f^2}{d} \tag{31}$$

where ϵ is the porosity, d is the particle diameter, and Δh is the effective bed height. At the onset of fluidization, the theoretical maximum pressure drop is given by:

$$\Delta p = (1-\epsilon)(\rho_p - \rho_f)g\Delta h \tag{32}$$

Fig. 16 presents the pressure drop as a function of inlet velocity. The numerical results agree well with the analytical solution in the fixed-bed regime and approach the theoretical limit upon fluidization. Slight deviations at high velocities (above 0.16 m/s) are likely due to particle rearrangement and local heterogeneity in the fluid pressure field.

Lastly, it is acknowledged that the present work does not include a formal convergence analysis in either space or time, which represents a clear limitation of the study. In particular, for transient flows with moving immersed boundaries, establishing the numerical order of accuracy remains essential for a complete verification framework. The primary focus of this work is to demonstrate the fidelity and applicability of the proposed hybrid CFD-DEM scheme across multiple resolution regimes, supported by representative tests against analytical, theoretical, and experimental references. Nonetheless, we recognize that this cannot substitute for a systematic order-of-accuracy assessment. Constructing manufactured solutions under such conditions is technically nontrivial, especially due to the difficulty in maintaining consistency between velocity, pressure, and forcing fields in fractional-step solvers such as PISO. Recent studies, such as Barbeau et al. [23], have proposed high-order immersed boundary formulations coupled with analytically tractable solutions that offer a viable path forward for convergence verification. Although such methodologies have not yet been implemented in our framework, they represent a valuable direction for future development, and this limitation is explicitly acknowledged herein.

5. Primary case study: Filtration in granular media

This section presents a detailed case study of fine particle filtration through a coarse granular medium to evaluate the performance of the proposed hybrid CFD-DEM framework. The simulation results are compared with those obtained from single-resolution CFD-DEM schemes to examine the effectiveness of the hybrid coupling strategy. In addition, the effects of particle shape and particle size on filtration behavior are analyzed, to demonstrate the geometric adaptability and multiscale capability of the framework.

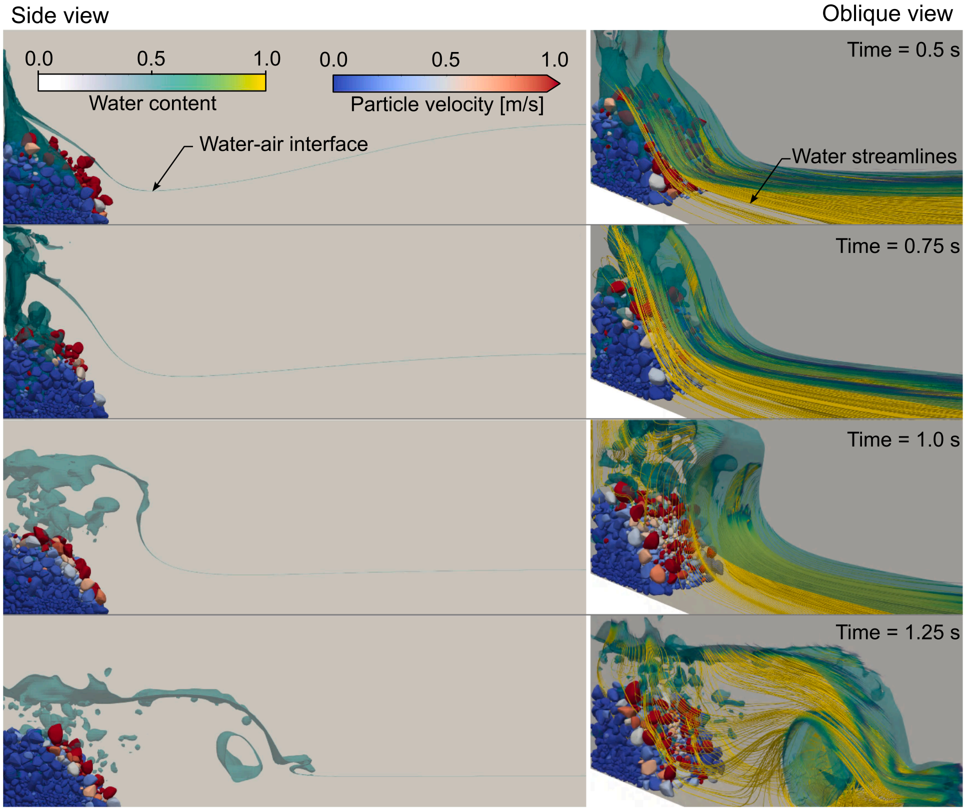

(a) Initial impact of dam-break wave

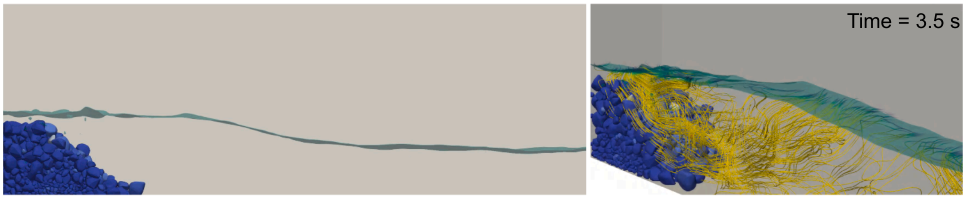

(b)Secondary impact of dam-break wave

(c)Tertiary round impact of dam-break wave

Fig. 39. Impact dynamics and granular velocity fields of the dam-break case. Snapshots of (a) initial, (b) secondary and (c) tertiary impacts.

5.1. Model setup

The model setup is illustrated in Fig. 17. Initially, a packing of coarse particles is generated via a dry DEM simulation. The particles are inserted into a box container and are then allowed to settle down under gravity. After reaching equilibrium, excess particles are removed to form a cubic coarse granular media measuring 0.4 m on each side. Subsequently, fine particles are introduced into the left side of the coarse grains, and finally, the model is input into the CFD-DEM solver for filtration simulation. The fluid domain in the CFD-DEM model is a cuboid measuring 1.2 m by 0.4 m by 0.4 m. Inlet boundary conditions are set on the left side, with the right side as an outlet; the lateral four side walls are defined as slip boundaries. Alongside these lateral fluid boundaries, four plane walls are inserted into the DEM scene to confine particle movement within the fluid stream. The coarse grains remain fixed, allowing only fine particles to move and enabling the study of the filtration process under controlled conditions. Linear contact is used and key model parameters are summarized in Table 2 .

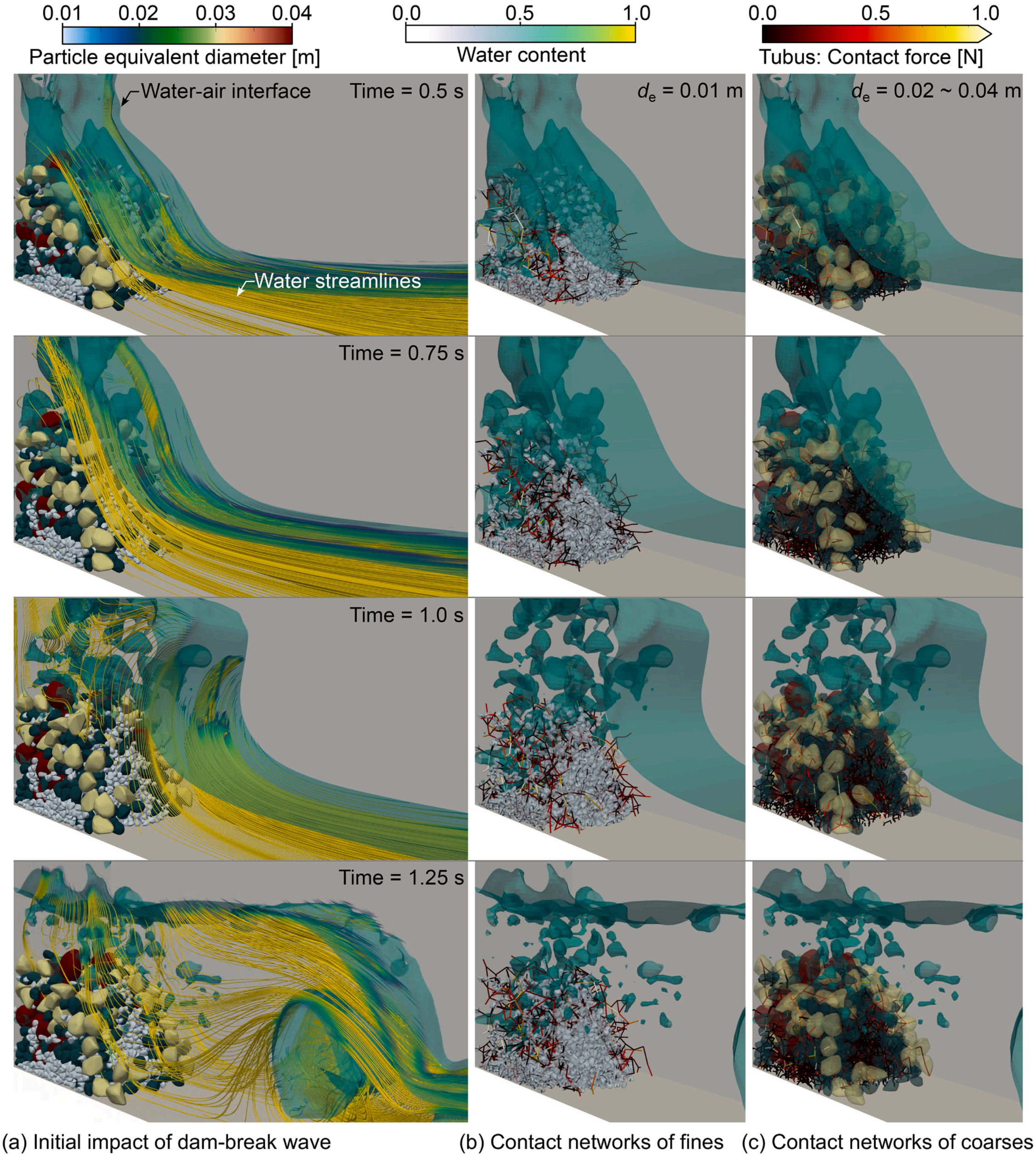

Fig. 40. Impact dynamics and contact networks during (a) initial dam-break-impact, and evolving contact networks with (b) fine and (c) coarse particles.

5.2. General results

The general results of the filtration simulation are presented first, where the coarse particles exhibit irregular shapes and the particle size ratio between coarse and fine particles is 10. Fig. 18 illustrates the spatial distribution of fine particles within the coarse granular media at the end of simulation. Initially injected on the left side, the fine particles tend to accumulate near the inlet region. Throughout filtration, some particles traverse deep into the coarse media, while others remain within it. Fig. 18(b) shows a generally uniform distribution of fine particles among the coarse media. Additionally, Fig. 19 presents the trajectories of fine particles during the simulation. The trajectories depict the intricate and convoluted paths that the fine particles take as they navigate through the porous structure formed by the coarse media.

The hydrodynamic behavior during the filtration process is analyzed by investigating the fluid velocity field and streamlines within the CFD domain, as shown in Fig. 20. Initially, the fluid velocity field exhibits a relatively uniform distribution, with slightly higher velocities within the coarse granular media region. However, as the filtration progresses, a noticeable increase in fluid velocity occurs within this region and at the outlet. This increase is attributed to the infiltration of fine particles into the media, reducing effective porosity and increasing flow resistance. Consequently, fluid flows through narrower pathways, leading to localized velocity accelerations within the media. Moreover, disorganized fluid streamlines are observed in the coarse granular media and outlet region by the end of the filtration simulation. This disorganization results from interactions among fine particles, fluid, and coarse media, perturbing flow patterns. The interaction generates localized disturbances and eddies in streamline patterns, reflecting the complex nature of fluid-particle interactions during filtration.

5.3. Effectiveness of the hybrid framework

To evaluate the effectiveness of the proposed hybrid CFD-DEM framework in multiscale filtration simulations, we conducted comparative tests against single resolved and single unresolved CFD-DEM approaches, using the same fluid mesh across all cases. As detailed in Section 2, the mesh is sufficiently refined to resolve the geometry and surface flow around coarse particles, which span approximately 8 fluid cells in diameter. However, this resolution is not adequate for resolving the flow field around fine particles, whose diameters are comparable to or smaller than the fluid cell size. In the single unresolved CFD-DEM simulation, coarse particles are treated with empirical drag models despite their size being significantly larger than the mesh. This mismatch leads to inaccurate estimates of porosity, velocity, and pressure in the fluid cells containing the particles, resulting in erroneous fluid-solid interaction forces and unphysical flow patterns. Conversely, the single resolved CFD-DEM simulation attempts to integrate surface stresses over the fine particle geometry. Yet, due to insufficient mesh resolution near these small particles, pressure and velocity gradients are poorly captured, which undermines the accuracy of the computed hydrodynamic force. The hybrid approach avoids these pitfalls by applying resolved coupling for coarse particles and sub-grid drag models for fine particles. This strategy ensures that each particle scale is treated with a numerically consistent method appropriate to the available resolution.

Fig. 21 shows the results of streamlines and fine particle filtration for the three approaches, highlighting distinct characteristics. The unresolved CFD-DEM generates streamlines that appear unrealistic, as they traverse directly through the coarse particle bodies. This discrepancy arises from the use of a relatively small fluid grid size in the unresolved CFD-DEM method, leading to inaccurate force calculations for the coarse particles. In contrast, both the resolved CFD-DEM and the hybrid CFD-DEM produce consistent flow streamline results. They accurately simulate the flow of fluid through the pores between the coarse particles, effectively capturing the particle-induced flow disturbances. However, at the end of the simulation, a significant number of fine particles fail to reach the region occupied by the coarse particle media in the resolved approach. This phenomenon may due to the use of a relatively large fluid grid size that results in inaccurate force calculations for the fine particles.

As a quantitative comparison, Fig. 22 presents the probability distribution of the x-component of fluid-particle interaction forces acting on fine particles within the coarse granular domain, as obtained from the hybrid and resolved CFD-DEM simulations. The resolved approach exhibits a sharp peak centered near-zero force, indicating that a large fraction of fine particles experience negligible hydrodynamic interaction. This artifact stems from insufficient mesh resolution around the fine particles, which prevents accurate reconstruction of local pressure and velocity gradients, leading to severely under-resolved surface stress integration. In contrast, the hybrid CFD-DEM simulation shows a broader and smoother force distribution. By applying empirical drag models, which remain valid even under coarser flow discretization, the hybrid approach yields more physically realistic estimates of fluid-particle interaction forces across the fine particle population. These results do not imply that the hybrid method is fundamentally more accurate than the resolved approach. Rather, they highlight that, under-resolved conditions such as those in the present setup, the resolved scheme fails to capture the necessary near-particle flow features, while the hybrid treatment remains robust. We emphasize that, on sufficiently refined meshes, a fully resolved approach would be expected to outperform hybrid formulations.

5.4. Effect of particle shape

To investigate the effect of particle shape on filtration, the filtration simulation are conducted using two sets of coarse particles, namely irregularly-shaped and spherical-shaped. The fine particles are kept spherical. Fig. 23 provides a visual comparison of how fine particles interact with these different types of coarse particles during filtration. For the case of spherical coarse particles, fewer fine particles are observed to get trapped within the media. These trapped fine particles tend to accumulate near the outlet region, suggesting a relatively lower capacity of spherical particles to retain fine particles throughout the media. On the other hand, in simulations with irregularly-shaped coarse particles, a higher number of fine particles are found trapped within the coarse granular media. Moreover, these fine particles are more evenly distributed throughout the media, indicating a greater capacity of irregularly-shaped particles to retain fine particles compared to their spherical counterparts.

The ratio of fine particles retaining within the coarse media over time, as depicted in Fig. 24, provides valuable insights into how different shapes of coarse grains impact the filtration process. Herein, the retaining ratio is defined as the ratio of the number of fine particles retained within the coarse granular media to the total number of fine particles present at any given moment during the simulation. A lower retaining ratio indicates a higher propensity for fine particles to bypass the coarse media. As the simulation progresses, the retaining ratio increases. Spherical coarse particles exhibit a lower retaining ratio compared to irregularly-shaped particles. This difference can be attributed to the smoother surfaces of spherical particles, which provide fewer entrapment sites for fine particles. In contrast, irregularly-shaped particles offer more irregularities and crevices, enhancing their ability to retain fine particles within the media.

Fig. 25 illustrates the fluid velocity field within the coarse particle region for both irregularly shaped and spherical particles. While the overall magnitude of the flow velocity remains comparable between the two cases, distinct differences emerge in the local flow patterns. The irregularly shaped particles create a more tortuous and geometrically complex pore network, which induces pronounced local flow disturbances, including recirculation zones and velocity deflections, as seen in Fig. 25(a). These effects arise from surface irregularities and pore-scale heterogeneity that disrupt the streamwise flow. In contrast, the spherical particle assembly results in a more ordered pore structure, with streamlines that are smoother and more aligned with the principal flow direction, as shown in Fig. 25(b). These qualitative observations suggest that particle shape plays a significant role in modulating local flow features, even under globally similar boundary conditions.

To quantitatively support these observations, we extracted the fluid velocity and pressure values from all CFD cells within the coarse particle region and computed their probability density functions, as shown in Fig. 26. The velocity distributions for both cases are relatively similar in magnitude, which is consistent with the imposed uniform inlet condition. However, the pressure distribution for the irregular case exhibits a broader tail and higher extreme values, indicating increased flow resistance and steeper pressure gradients caused by the irregular pore geometry. These statistical results quantitatively confirm that shape-induced heterogeneity manifests more strongly in pressure variations than in velocity magnitude. Future investigations may incorporate additional descriptors, such as directional velocity variance, shear rate, vorticity, or Lagrangian flow paths, to further characterize the anisotropy and complexity of pore-scale transport in geometrically heterogeneous media.

5.5. *Effect of particle size*

To investigate the effect of particle size on the filtration process, six different coarse to fine particle size ratios (5, 6, 7, 8, 9, and 10) are considered. Fig. 27 visually presents the position of fine particles at the end of the filtration simulation for each particle size ratio. An intriguing trend emerges from these observations: as the particle size ratio decreases, the fine particles tend to be more readily captured within the filtration system. This phenomenon can be rationalized by considering the increased likelihood of fine particles encountering and becoming trapped by the larger surface area provided by a higher concentration of coarse particles. Fig. 28 quantitatively illustrates this trend by depicting the retaining ratio for each particle size ratio. Notably, the retaining ratio for a particle size ratio of 5 is approximately three times as high as that for a particle size ratio of 10, highlighting the significant impact of particle size on the efficiency of particle capture within the filtration setup.

To deepen our understanding of the fine particle distribution within the coarse media, we segmented the coarse granular media into three distinct regions along the flow direction: left, middle, and right sections. It allows to analyze how the distribution of fine particles varies across these regions, particularly concerning different particle size ratios. Fig. 29 provides valuable insights into this distribution. For instance, when considering a particle size ratio of 5, a notable concentration of fine particles is observed in the left region, which is closer to the inlet. This concentration diminishes as it moves towards the middle and right sections. Interestingly, as the particle size ratio increases, the distribution of fine particles becomes more uniform across the entire coarse media. This uniformity suggests that the larger spaces between coarse particles facilitate the dispersion of fine particles throughout the media.

To further examine the influence of particle size ratio on local flow behavior, we analyzed the fluid velocity field within the porous medium under varying coarse-to-fine particle size ratios. As shown in Fig. 30, the overall flow structure remains relatively consistent across the tested size ratios, with only minor visual variations observed in the velocity distribution. Under the current configuration and boundary conditions, the particle size ratio appears to have limited influence on the bulk flow dynamics within the filtration region. Given the similarity in the flow patterns, and in line with the findings in Fig. 25, we omit a separate statistical analysis for brevity. The earlier results in Fig. 26 have already demonstrated that particle shape, rather than size ratio, plays a more decisive role in inducing local flow heterogeneity. Based on the particle size distributions considered in this study and the corresponding flow responses, the observed insensitivity to size ratio suggests a degree of geometric robustness, which may be beneficial in the design of filtration systems aiming for consistent flow environments across a range of configurations. Although velocity magnitude distributions provide useful first-order insight, a more detailed characterization of pore-scale flow complexity may be achieved through additional metrics. Future work may consider the use of directional velocity variance, vorticity and shear rate fields, or Lagrangian flow path analysis to better capture the spatial anisotropy and transport heterogeneity arising from geometric effects.

6. Extended case studies: Granular flow and multiscale interactions

This section presents three extended case studies to demonstrate the scalability and versatility of the proposed hybrid CFD-DEM framework. These examples span a range of fluid-particle systems, including particle sorting in channelized transport, jet-induced destabilization in granular media, and dam break flow impacting granular bed. While detailed physical process analyses are not the focus here, these cases illustrate the generalizability of the framework for complex, geometry-sensitive simulations involving multiscale fluid-particle interactions. Unless otherwise specified, most of the fluid and particle properties follow those used in the previous filtration example. For all extended case studies, linear contact model is used and the normal and tangential contact stiffness are consistently set to 2.0×10^4 N/m and 1.0×10^4 N/m, respectively, as a compromise to accelerate computation while maintaining physically reasonable contact behavior.

6.1. Particle sorting in channelized transport

Particle sorting is a fundamental mechanism in gravity-driven granular flows such as debris flows, landslides, and sediment transport, where differences in particle size or density induce spatial sorting and stratification. To demonstrate the capability of the proposed hybrid CFD-DEM framework in capturing such behavior, a numerical model is developed based on the dry chute-flow experiments conducted by Sheng et al. [89]. In contrast to the original dry setup, the present model incorporates fluid flow and focuses on simulating sorting driven by both hydrodynamic and gravitational forces in a bidisperse granular system. As illustrated in Fig. 31, the granular column consists of coarse irregular-shaped particles with an equivalent diameter of 0.02 m and fine spherical particles with a diameter of 0.01 m. These particles are initially confined within a box measuring 0.5 m in width and 0.4 m in height. The base is composed of fixed spherical particles with a diameter of 0.012 m, arranged in a regular pattern to mimic the roughened basal surface used in laboratory experiments. A horizontal water flow with a constant inlet velocity of 0.1 m/s enters from the left boundary, interacting with the granular column. The fluid domain measures 2.5 m by 0.06 m by 0.1 m and is discretized into a structured mesh of 1000 by 24 by 40 cells. Gravity is inclined at 45° from the horizontal to simulate downslope transport. The coarse and fine particles are released by numerically removing a confining gate. The contact friction and damping are set to 0.3, respectively. This setup retains the essential mechanisms of dry sorting while enabling detailed investigation of fluid-induced effects and shape-dependent behaviors under hybrid coupling.

Fig. 32 illustrates the dynamic process of size-induced particle sorting during CFD-DEM simulation, with particles colored by equivalent diameter. Initially, coarse irregular particles and fine spherical particles are well mixed within the granular column. Upon gate removal, the mixture is released and subjected to a horizontal water flow combined with gravity inclined at 45°, simulating downslope transport. As the flow progresses, fine particles gradually percolate downward, while coarse particles migrate upward, leading to a clear stratification. By $t = 10.0$ s, a layered structure emerges, with coarse particles concentrated near the surface and fine particles forming the lower layers, as highlighted in the zoom-in view. The evolution of particle velocities and fluid streamlines during the sorting process is shown in Fig. 33. In the initial stage, the fluid flow interacts with the packed granular column, generating fast fluid channels near the base. As the granular is released and flows downslope under inclined gravity and fluid drag, both fluid and particle motions become highly dynamic. As time progresses, strong fluid-particle interactions give rise to complex flow structures, including localized recirculation and streamline bending. This complex and disordered flow may suppress or delay the particle sorting process. These results highlight the ability of the hybrid resolved and unresolved CFD-DEM approach to capture typical sorting behavior arising from size disparity under coupled fluid-particle interactions.

To quantify the degree of sorting, the average height difference between coarse and fine particles is calculated. Coarse and fine groups are defined by particle equivalent diameter, and their mean vertical positions are compared. The analysis is conducted in a region near the run-out front, extending 0.5 m in length and starting 0.25 m from the release gate. This region is chosen due to its relatively stable flow and the clear manifestation of particle sorting. The temporal evolution of the sorting index is presented in Fig. 34. At the initial stage, the difference remains close to its baseline, indicating limited separation between coarse and fine particles. As time progresses, the difference gradually increases as coarse particles migrate upward and fine particles move downward. Between 3 and 6 s, the increase becomes more pronounced, reflecting the progressive development of sorting. After 6 s, the growth becomes more significant, and a clear inverse grading pattern is formed. Overall, the simulation successfully captures key features of particle sorting under coupled flow conditions and demonstrates the ability of the hybrid CFD-DEM framework to resolve the multiscale interplay between particle size, shape, and fluid motion in channelized granular transport.

6.2. Jet-induced destabilization in granular media

The jet-induced destabilization example mimics internal instability processes, such as those observed in piping failures, where upward seepage mobilizes particles and compromises structural stability. The simulation domain is defined as a rectangular cuboid measuring 0.15 m in length, 0.03 m in width, and 0.20 m in height. The lower 0.10 m of the domain is filled with a granular packing composed of particles with equivalent diameters of 0.3 cm, 0.5 cm, 1.0 cm, and 1.5 cm, randomly mixed to mimic natural heterogeneity. Approximately 35,000 particles are deposited through gravitational settling in a confined dry DEM simulation. The fluid phase is resolved using a structured mesh of 150 by 30 by 200 cells, ensuring sufficient spatial resolution for both pore-scale and bulk interactions. At the onset of the simulation, the bottom 0.05 m of the domain is saturated with water, while the upper portion remains occupied by air, establishing a two-phase flow environment. A square jet inlet, 3 cm by 3 cm, is positioned centrally at the bottom boundary and injects water vertically upward at a constant speed of 3 m/s. Slip boundary conditions are applied to the bottom 0.10 m of the side walls, while the top 0.10 m are defined as pressure outlets with zero gauge pressure, allowing fluid and mobilized particles to exit freely. This configuration generates a localized high-shear zone beneath the granular bed, inducing progressive fluidization and particle entrainment. As illustrated in Fig. 35, the particle and fluid domains are visualized using half-section views to highlight the internal configuration and injection region.

Figs. 36 and 37 illustrate the coupled evolution of free surface deformation, particle mobilization, and internal contact force redistribution during jet-induced destabilization. In the early stage ($t < 1.0$ s), the fluid jet locally perturbs the packing, while the free surface rises smoothly, modulated by the geometry of overlying coarse particles. The interaction between fluid velocity gradients and particle shape induces asymmetric surface undulations and entrains small air bubbles, demonstrating the good capability of the framework in resolving fluid-air-solid three-phase interfaces. As the upward shear intensifies, particles are gradually eroded from the jet core, and the entrained region transitions from a narrow vertical column to a fan-shaped zone. This reflects the shift from a localized force-dominated regime to a broader fluidization-dominated flow field. Meanwhile, particle trajectories exhibit size-dependent sorting, i.e., larger particles tend to remain near the injection zone base, while smaller particles are lifted and redistributed to the upper layers. The corresponding force chain evolution (see Fig. 37) reveals the internal mechanical response underpinning this process. Initially, strong force chains support the overburden, concentrated in vertical columns. With fluid penetration, these load-bearing paths gradually weaken and break apart, particularly in the jet core. Lateral chains near the flanks remain active for a longer duration, sustaining localized shear resistance. As erosion progresses, the force network becomes sparse and fragmented, signaling the collapse of structural stability. This complex interplay between local flow structures, particle-scale interactions, and global force redistribution underscores the necessity of a hybrid resolved-unresolved approach that can consistently capture shape-sensitive contact mechanics and multiscale fluid-solid coupling within a unified numerical framework.

6.3. Dam-break flow impacting granular bed

This example simulates a dam-break wave impinging on a well-graded granular bed to examine fluid-granular coupling under transient flow conditions. As shown in Fig. 38, the simulation domain consists of a rectangular tank measuring 1.5 m by 0.2 m by 0.5 m. The fluid domain is initially divided into water and air regions, with the right-side region filled with a column of water and the rest occupied by air. The CFD domain is bounded by five no-slip walls and an atmospheric top boundary, while the DEM boundaries include frictional rigid walls on the base and sides. The granular bed is constructed by randomly generating 2400 irregular particles of four sizes (0.01 m, 0.02 m, 0.03 m, and 0.04 m in equivalent diameter), mixed in equal mass fractions to form a polydisperse assembly. The particles are first deposited via a dry settling process under gravity. Fig. 38(b) illustrates the relative sizes of the particles compared to the CFD mesh resolution.

The movement and contact networks of granular materials during granular-fluid interactions have been extensively studied in recent literature [90,91]. Fig. 39 illustrates the impact dynamics and granular velocity fields for the dam-break scenario. To elucidate the complex behaviors of dam-break waves interacting with polydisperse irregular-shaped particles, water streamlines and particle velocities are visualized throughout the simulation. Fig. 39(a) shows the initial impact of the dam-break wave at 0.5, 0.75, 1.0, and 1.25 seconds, capturing phenomena such as runup, overtopping, back-roll waves, and the formation of entrapped bubbles in the porous medium. The movement of smaller particles through the pore spaces of the well-graded sample is also clearly observed during wave impact. Fig. 39(b) and (c) depict the secondary and tertiary impacts, respectively. As the wave energy dissipates through successive interactions with the granular bed, the water streamlines exhibit progressively reduced complexity, particularly during the tertiary impact. These results demonstrate that the proposed hybrid CFD-DEM method effectively captures the intricate interactions between water and irregular polydisperse particles in dam-break conditions.

In parallel, Fig. 40 presents the evolution of contact networks during the initial wave impact. The hybrid framework enables a detailed investigation of how particles of different sizes contribute to the formation and evolution of contact structures within a polydisperse granular bed. Specifically, Fig. 40(b) and (c) highlight the role of small and large particles, respectively, in shaping the dynamic contact topology during impact. To the authors' knowledge, this is the first instance where hydro-mechanical simulations explicitly resolve the contribution of irregularly-shaped particles of varying sizes to contact network evolution under dam-break conditions. While a comprehensive quantitative analysis of these effects is beyond the present scope, the results shown here, along with the supporting animation, offer clear evidence of such interactions and their spatiotemporal evolution. It is noted that while numerous studies have examined dam-break flows with uniform spherical or non-spherical particles (e.g., [92,93]), experiments involving well-graded, irregular sediments often pertain to engineering applications where detailed particle-scale data, such as particle number, shape, and size distribution, are quite limited (e.g., [94,95]). Future work will include well-designed experiments to provide rigorous validation for these complex fluid-solid systems involving widely graded, irregular particles.

7. Summary

This study has developed a flexible hybrid CFD-DEM framework for simulating fluid-particle systems involving irregularly shaped and polydisperse particles. By integrating resolved, semi-resolved, and unresolved coupling strategies within a unified architecture, the framework enables accurate and efficient modeling of multiscale particle-fluid interactions. Key methodologies, including signed distance field (SDF)-based particle representation, coarse-graining techniques, and a point-sphere contact model for coarse-fine interactions, have been introduced and implemented. The proposed solver has been verified through classical benchmark tests, including wedge water-entry, particle settling and Ergun's packed bed, demonstrating its accuracy and reliability. A comprehensive filtration case study further illustrates the capacity of the framework to capture the effects of particle shape and size on migration and clogging behavior. Additional case studies involving channelized granular sorting, jet-induced destabilization, and dam break flow highlight its scalability and applicability to diverse engineering scenarios. Overall, the hybrid CFD-DEM framework provides a generalizable and geometry-aware computational tool for investigating complex fluid-particle systems. Future work will extend validation and application to a broader range of environmental and engineering processes involving particle transport and structural evolution.

CRediT authorship contribution statement

Zhengshou Lai: Writing – original draft, Visualization, Software, Investigation, Formal analysis, Conceptualization; **Shuai Huang:** Investigation, Formal analysis, Data curation; **Yong Kong:** Investigation, Formal analysis, Data curation; **Shiwei Zhao:** Visualization, Investigation; **Jidong Zhao:** Writing – review & editing, Supervision, Funding acquisition; **Linchong Huang:** Writing – review & editing, Project administration, Funding acquisition.

Data availability

Data will be made available on request.

Declaration of competing interest

The authors declare that they have no known competing financial interests or personal relationships that could have appeared to influence the work reported in this paper.

Acknowledgement

This work was financially supported by the Guangdong Major Project of Basic Research (2025B0303000011), the National Natural Science Foundation of China (52478428, 52439001), and the Research Grants Council of Hong Kong (GRF 16203123, CRF C7085-24G, RIF R6008-24, TRS T22-607/24-N).

Appendix A. Formulation of SDF-DEM

In the SDF-DEM framework [44], each particle is represented by a signed distance function (SDF), $\Phi(\vec{x}) : \mathbb{R}^3 \rightarrow \mathbb{R}$, with the convention that $\Phi > 0$ inside the particle and $\Phi < 0$ outside; the particle surface corresponds to the zero-th level set. Two basic primitives are required: evaluation of $\Phi(\vec{x})$ at an arbitrary point and a surface projection operator $\Pi(\cdot)$ that maps a point to its closest location on the particle surface. A node-to-surface strategy is used for contact detection and resolution. For a particle pair (A, B), the SDF of particle A is used to detect intrusion, while the surface of particle B is discretized by surface nodes. A contact is activated at any surface node P_i of B for which $\Phi_A(\vec{x}_{P_i}) > 0$.

Normal contact forces are derived from a distance-potential formulation to ensure energy consistency. Let particle A serve as the reference, and denote the configuration of particle B by its position $\vec{x}$ and orientation $\vec{\theta}$. The normal force $\vec{F}_n$ and moment $\vec{M}_n$ are given by

$$\vec{F}_n = -\frac{\partial w}{\partial \vec{x}}, \qquad \vec{M}_n = -\frac{\partial w}{\partial \vec{\theta}} \tag{A.1}$$

where $w(\vec{x}, \vec{\theta})$ denotes the total contact potential. The resulting force can be projected to a physical contact location as

$$\vec{x}_c = \frac{\vec{n} \times \vec{M}_n}{F_n} + \lambda \vec{n}, \qquad \vec{n} = \vec{F}_n / F_n \tag{A.2}$$

with λ a free scalar controlling the location along the normal direction.

Each node is assumed to carry a contact potential. Thereby, the nodal contributions to the total force are evaluated over intruding nodes $P_i \in B \rightarrow A$ as

$$\vec{F}_n = \sum_i \vec{F}_{n,i} \tag{A.3}$$

$$\vec{F}_{n,i} = -\mathcal{F}'(d_i) \frac{\partial d_i}{\partial \vec{x}} \tag{A.4}$$

where $\mathcal{F}(d_i)$ is the contact potential function, $d_i = \Phi_A(\vec{x}_{P_i})$ is the SDF value at the contact node, and the gradient is approximated via finite differences. Details of the contact potential functions, including formulations for linear and Hertzian models, can be found in [57].

Tangential interactions are modeled using a bi-directional linear spring with Coulomb friction at each active node. To ensure that the accumulated tangential displacement remains orthogonal to the evolving contact normal during long-lasting collisions, the tangential force history is updated incrementally in the local contact frame. At each time step, once the contact normal is updated, the tangential force from the previous step is rotated into the new tangential plane while preserving its magnitude. The current relative tangential displacement is then projected onto the updated local tangential directions and used to increment the rotated tangential force. This procedure prevents the accumulation of non-orthogonal components and ensures consistency throughout the contact duration. Let $\vec{s}, \vec{t}, \vec{n}$ be an orthonormal basis of the contact plane, where $\vec{t} = \vec{s} \times \vec{n}$. The tangential forces evolve in an incremental manner as

$$F_s = F_s^* - k_t \delta_s \qquad F_t = F_t^* - k_t \delta_t \tag{A.5}$$

where * denotes the previous step and k_t is the tangential stiffness. Frictional displacements are computed from the relative surface velocity at the contact point:

$$\delta_s = (\vec{v}_{\text{rel}} \cdot \vec{s}) \Delta t, \qquad \delta_t = (\vec{v}_{\text{rel}} \cdot \vec{t}) \Delta t \tag{A.6}$$

$$\vec{v}_{\mathrm{rel}} = \vec{v}_{c_A} - \vec{v}_{c_B} + \vec{\omega}_A \times \vec{b}_A - \vec{\omega}_B \times \vec{b}_B \tag{A.7}$$

where $\vec{b}_A$ and $\vec{b}_B$ are the branch vectors from particle centroid to contact point. Coulomb friction is imposed via a projection:

$$F'_{st,i} = \min\left(\sqrt{F_{s,i}^2 + F_{t,i}^2}, \mu F_{n,i}\right) \tag{A.8}$$

$$F'_{s,i} = F'_{st,i} \frac{F_{s,i}}{\sqrt{F_{s,i}^2 + F_{t,i}^2}}, \qquad F'_{t,i} = F'_{st,i} \frac{F_{t,i}}{\sqrt{F_{s,i}^2 + F_{t,i}^2}} \tag{A.9}$$

where μ is the coefficient of friction. This formulation is suitable for monotonic or quasi-static loading; more advanced models may be needed to capture complex cyclic behavior. Details of the definition and update of contact plane can be found in Lai et al. [45].

Supplementary material

Supplementary material associated with this article can be found, in the online version, at 10.1016/j.jcp.2026.114759

References

[1] A.T. Williams, N. Rangel-Buitrago, E. Pranzini, G. Anfuso, The management of coastal erosion, Ocean Coastal Manage. 156 (2018) 4–20.
[2] E. Akhlaghi, M.S. Babarsad, E. Derikvand, M. Abedini, Assessment the effects of different parameters to rate scour around single piers and pile groups: a review, Arch. Comput. Methods Eng. 27 (1) (2020) 183–197.
[3] R.A.M. Putra, D. Pratiwi, A.D. Putra, E.P. Wahono, D.I. Kusumastuti, A. Fitri, Hydraulic gradient analysis on embankment dam foundation associated with internal erosion, in: IOP Conference Series: Earth and Environmental Science, 1173, IOP Publishing, 2023, p. 012027.
[4] A. Toimil, P. Camus, I.J. Losada, G. Le Cozannet, R.J. Nicholls, D. Idier, A. Maspataud, Climate change-driven coastal erosion modelling in temperate sandy beaches: methods and uncertainty treatment, Earth Sci. Rev. 202 (2020) 103110.
[5] J. Yang, Z.-Y. Yin, F. Laouafa, P.-Y. Hicher, Modeling coupled erosion and filtration of fine particles in granular media, Acta Geotech. 14 (2019) 1615–1627.
[6] S. Hube, M. Eskafi, K.F. Hrafnkelsdóttir, B. Bjarnadóttir, M. Bjarnadóttir, S. Axelsdóttir, B. Wu, Direct membrane filtration for wastewater treatment and resource recovery: a review, Sci. Total Environ. 710 (2020) 136375.
[7] F. Khamitov, N.H. Minh, Y. Zhao, Coupled CFD–DEM numerical modelling of perforation damage and sand production in weak sandstone formation, Geomechan. Energy Environ. 28 (2021) 100255.
[8] N. Li, X. Lu, M. He, X. Duan, B. Yan, G. Chen, S. Wang, Catalytic membrane-based oxidation-filtration systems for organic wastewater purification: a review, J. Hazard. Mater. 414 (2021) 125478.
[9] Y. Yin, Y. Cui, L. Jing, Clogging and unclogging of fine particles in porous media: micromechanical insights from an analog pore system, Water Resour. Res. 60 (1) (2024) e2023WR034628.
[10] P. Kieckhefen, S. Pietsch, M. Dosta, S. Heinrich, Possibilities and limits of computational fluid dynamics–discrete element method simulations in process engineering: a review of recent advancements and future trends, Annu. Rev. Chem. Biomol. Eng. 11 (1) (2020) 397–422.
[11] M.A. El-Emam, L. Zhou, W. Shi, C. Han, L. Bai, R. Agarwal, Theories and applications of CFD–DEM coupling approach for granular flow: a review, Arch. Comput. Methods Eng. 28 (7) (2021) 4979–5020.
[12] C. Kloss, C. Goniva, A. Hager, S. Amberger, S. Pirker, Models, algorithms and validation for opensource DEM and CFD–DEM, Progr. Comput. Fluid Dyn. An Int. J. 12 (2-3) (2012) 140–152.
[13] J. Zhao, T. Shan, Coupled CFD–DEM simulation of fluid–particle interaction in geomechanics, Powder Technol. 239 (2013) 248–258.
[14] T. Shan, J. Zhao, A coupled CFD-DEM analysis of granular flow impacting on a water reservoir, Acta Mech. 225 (2014) 2449–2470.
[15] Z. Wang, M. Liu, Semi-resolved CFD–DEM for thermal particulate flows with applications to fluidized beds, Int. J. Heat Mass Transfer 159 (2020) 120150.
[16] H.H. Hu, N.A. Patankar, M.Y. Zhu, Direct numerical simulations of fluid–solid systems using the arbitrary Lagrangian–Eulerian technique, J. Comput. Phys. 169 (2) (2001) 427–462.
[17] C.S. Peskin, The immersed boundary method, Acta Numerica 11 (2002) 479–517.
[18] A.N. Balachandran Nair, S. Pirker, T. Umundum, M. Saeedipour, A reduced-order model for deformable particles with application in bio-microfluidics, Comput. Partic. Mechan. 7 (2020) 593–601.
[19] T. Yu, J. Zhao, Semi-coupled resolved CFD–DEM simulation of powder-based selective laser melting for additive manufacturing, Comput. Methods Appl. Mech. Eng. 377 (2021) 113707.
[20] Z. Shen, G. Wang, D. Huang, F. Jin, A resolved CFD-DEM coupling model for modeling two-phase fluids interaction with irregularly shaped particles, J. Comput. Phys. 448 (2022) 110695.
[21] Z. Zeng, J. Fu, Y.T. Feng, M. Wang, Revisiting the empirical particle-fluid coupling model used in DEM-CFD by high-resolution DEM-LBM-IMB simulations: a 2D perspective, Int. J. Numer. Anal. Methods Geomech. 47 (5) (2023) 862–879.
[22] R. Verzicco, Immersed boundary methods: historical perspective and future outlook, Annu. Rev. Fluid Mech. 55 (1) (2023) 129–155.
[23] L. Barbeau, S. Golshan, J. Deng, S. Étienne, C. Béguin, B. Blais, High-order moving immersed boundary and its application to a resolved CFD-DEM model, Comput. Fluids 268 (2024) 106094.
[24] K. Cheng, Y. Wang, Q. Yang, A semi-resolved CFD-DEM model for seepage-induced fine particle migration in gap-graded soils, Comput. Geotech. 100 (2018) 30–51.
[25] Z. Wang, Y. Teng, M. Liu, A semi-resolved CFD–DEM approach for particulate flows with kernel based approximation and Hilbert curve based searching strategy, J. Comput. Phys. 384 (2019) 151–169.
[26] Q. Yang, K. Cheng, Y. Wang, M. Ahmad, Improvement of semi-resolved CFD-DEM model for seepage-induced fine-particle migration: eliminate limitation on mesh refinement, Comput. Geotech. 110 (2019) 1–18.
[27] G. Zhu, H. Li, Z. Wang, T. Zhang, M. Liu, Semi-resolved CFD-DEM modeling of gas-particle two-phase flow in the micro-abrasive air jet machining, Powder Technol. 381 (2021) 585–600.
[28] Z. Wang, M. Liu, On the determination of grid size/smoothing distance in un-/semi-resolved CFD-DEM simulation of particulate flows, Powder Technol. 394 (2021) 73–82.
[29] J. Chen, J. Zhang, A semi-resolved CFD-DEM coupling model using a two-way domain expansion method, J. Comput. Phys. 469 (2022) 111532.
[30] H. Che, K. Windows-Yule, C. O'sullivan, J. Seville, A novel semi-resolved CFD-DEM method with two-grid mapping: methodology and verification, AlChE J. 70 (2) (2024) e18321.
[31] J. Capecelatro, O. Desjardins, An Euler–Lagrange strategy for simulating particle-laden flows, J. Comput. Phys. 238 (2013) 1–31.
[32] M. Hausmann, V. Chéron, F. Evrard, B. Van Wachem, Study and derivation of closures in the volume-filtered framework for particle-laden flows, J. Fluid Mech. 996 (2024) A41.

[33] Z. Su, C. Xu, K. Jia, C. Cui, X. Du, A novel semi-resolved CFD-DEM coupling method based on point cloud algorithm for complex fluid-particle systems, Comput. Methods Appl. Mech. Eng. 434 (2025) 117561.
[34] T. El Geitani, B. Blais, Quadrature-centered averaging scheme for accurate and continuous void fraction calculation in computational fluid dynamics–discrete element method simulations, Industr. Eng. Chem. Res. 62 (12) (2023) 5394–5407.
[35] F. Evrard, F. Denner, B. van Wachem, Euler-Lagrange modelling of dilute particle-laden flows with arbitrary particle-size to mesh-spacing ratio, J. Comput. Phys. X 8 (2020) 100078.
[36] Q. Xiong, L. Deng, W. Wang, W. Ge, SPH method for two-fluid modeling of particle–fluid fluidization, Chem. Eng. Sci. 66 (9) (2011) 1859–1865.
[37] M. Riella, R. Kahraman, G.R. Tabor, Reynolds-averaged two-fluid model prediction of moderately dilute fluid-particle flow over a backward-facing step, Int. J. Multiphase Flow 106 (2018) 95–108.
[38] B. Esgandari, S. Rauchenzauner, C. Goniva, P. Kieckhefen, S. Schneiderbauer, A comprehensive comparison of two-fluid model, discrete element method and experiments for the simulation of single-and multiple-spout fluidized beds, Chem. Eng. Sci. 267 (2023) 118357.
[39] R.O. Fox, The particle–fluid–particle pressure tensor for ideal-fluid–particle flow, J. Fluid Mech. 1010 (2025) A8.
[40] S.T.W. Kuruneru, E. Marechal, M. Deligant, S. Khelladi, F. Ravelet, S.C. Saha, E. Sauret, Y. Gu, A comparative study of mixed resolved–unresolved CFD-DEM and unresolved CFD-DEM methods for the solution of particle-laden liquid flows, Arch. Comput. Methods Eng. 26 (2019) 1239–1254.
[41] Y. Wang, K. Cheng, Y. Yang, Y. Tao, Y. Li, Microscopic mechanical analysis of sand production using a new arbitrary resolved-unresolved CFD-DEM model, Int. J. Multiphase Flow 149 (2022) 103979.
[42] Z. Xie, S. Wang, Y. Shen, A novel hybrid CFD-DEM method for high-fidelity multi-resolution modelling of cross-scale particulate flow, Chem. Eng. J. 455 (2023) 140731.
[43] G. Hu, B. Zhou, W. Zheng, K. Cheng, H. Wang, A hybrid resolved CFD-DEM study on internal erosion in gap-graded soils considering coarse particle shape, Comput. Geotech. 183 (2025) 107204.
[44] Z. Lai, S. Zhao, J. Zhao, L. Huang, Signed distance field framework for unified DEM modeling of granular media with arbitrary particle shapes, Comput. Mech. 70 (2022) 763–783.
[45] Z. Lai, J. Zhao, S. Zhao, L. Huang, Signed distance field enhanced fully resolved CFD-DEM for simulation of granular flows involving multiphase fluids and irregularly shaped particles, Comput. Methods Appl. Mech. Eng. 414 (2023) 116195.
[46] S. Huang, L. Huang, Z. Lai, J. Zhao, Morphology characterization and discrete element modeling of coral sand with intraparticle voids, Eng. Geol. 315 (2023) 107023.
[47] S. Zhao, J. Zhao, Revolutionizing granular matter simulations by high-performance ray tracing discrete element method for arbitrarily-shaped particles, Comput. Methods Appl. Mech. Eng. 416 (2023) 116370.
[48] C. Zhang, SDFIBM: a signed distance field based discrete forcing immersed boundary method in OpenFOAM, Comput. Phys. Commun. 255 (2020) 107370.
[49] L. Barbeau, S. Etienne, C. Beguin, B. Blais, Development of a high-order continuous Glerkin sharp-interface immersed boundary method and its application to incompressible flow problems, Comput. Fluids 239 (2022) 105415.
[50] H. Ström, H. Luo, Q. Xiong, Perspectives on particle–fluid coupling at varying resolution in CFD-DEM simulations of thermochemical biomass conversion, Energy Fuels 38 (18) (2024) 17179–17190.
[51] S. Wang, Y. Shen, Coarse-grained CFD-DEM modelling of dense gas-solid reacting flow, Int. J. Heat Mass Transfer 184 (2022) 122302.
[52] Q. Sun, Q. Chen, Y. Xia, F. Chen, J. Klinger, L. Ding, V. Thompson, Reverse scaling of a bonded-sphere DEM model: formulation and application to lignocellulosic biomass microstructures, Powder Technol. 409 (2022) 117797.
[53] B. Jensen, N.G. Jacobsen, E.D. Christensen, Investigations on the porous media equations and resistance coefficients for coastal structures, Coastal Eng. 84 (2014) 56–72.
[54] C.W. Hirt, B.D. Nichols, Volume of fluid (VOF) method for the dynamics of free boundaries, J. Comput. Phys. 39 (1) (1981) 201–225.
[55] A. Albadawi, D.B. Donoghue, A.J. Robinson, D.B. Murray, Y. Delauré, Influence of surface tension implementation in volume of fluid and coupled volume of fluid with level set methods for bubble growth and detachment, Int. J. Multiphase Flow 53 (2013) 11–28.
[56] P. Bohorquez, Computational continuum mechanics for sediment transport in free-surface flow, in: Open Source CFD International Conference 2008, 2008, p. 17.
[57] Z. Lai, Y.T. Feng, J. Zhao, L. Huang, Unifying the contact in signed distance field-based and conventional discrete element methods, Comput. Geotech. 176 (2024) 106764.
[58] Z. Lai, Q. Chen, L. Huang, Machine-learning-enabled discrete element method: contact detection and resolution of irregular-shaped particles, Int. J. Numer. Anal. Methods Geomech. 46 (1) (2022) 113–140.
[59] S. Huang, P. Wang, Z. Lai, Z.-Y. Yin, L. Huang, C. Xu, Machine-learning-enabled discrete element method: the extension to three dimensions and computational issues, Comput. Methods Appl. Mech. Eng. 432 (2024) 117445.
[60] J. Mao, L. Zhao, Y. Di, X. Liu, W. Xu, A resolved CFD–DEM approach for the simulation of landslides and impulse waves, Comput. Methods Appl. Mech. Eng. 359 (2020) 112750.
[61] J. Yang, E. Balaras, An embedded-boundary formulation for large-eddy simulation of turbulent flows interacting with moving boundaries, J. Comput. Phys. 215 (1) (2006) 12–40.
[62] N. Hori, M.E. Rosti, S. Takagi, An Eulerian-based immersed boundary method for particle suspensions with implicit lubrication model, Comput. Fluids 236 (2022) 105278.
[63] S.H. Saraei, B. Peters, Immersed boundary method for considering lubrication effects in the CFD-DEM simulations, Powder Technol. 426 (2023) 118603.
[64] S.L. Dance, M.R. Maxey, Incorporation of lubrication effects into the force-coupling method for particulate two-phase flow, J. Comput. Phys. 189 (1) (2003) 212–238.
[65] A. Lefebvre-Lepot, B. Merlet, T.N. Nguyen, An accurate method to include lubrication forces in numerical simulations of dense Stokesian suspensions, J. Fluid Mech. 769 (2015) 369–386.
[66] D.J. Jeffrey, Low-Reynolds-number flow between converging spheres, Mathematika 29 (1) (1982) 58–66.
[67] I.N. Tsimpanogiannis, S.H. Jamali, I.G. Economou, T.J.H. Vlugt, O.A. Moultos, On the validity of the Stokes–Einstein relation for various water force fields, Mol. Phys. 118 (9-10) (2020) e1702729.
[68] H.R. Norouzi, R. Zarghami, R. Sotudeh-Gharebagh, N. Mostoufi, Coupled CFD-DEM Modeling: Formulation, Implementation and Application to Multiphase Flows, John Wiley & Sons, 2016.
[69] W. Sobieski, Switch function and sphericity coefficient in the Gidaspow drag model for modeling solid-fluid systems, Drying Technol. 27 (2) (2009) 267–280.
[70] S. Ergun, A.A. Orning, Fluid flow through randomly packed columns and fluidized beds, Industr. Eng. Chem. 41 (6) (1949) 1179–1184.
[71] C.Y. Wen, Y.H. Yu, A generalized method for predicting the minimum fluidization velocity, AlChE J. 12 (3) (1966) 610–612.
[72] U. Lei, C.Y. Yang, K.C. Wu, Viscous torque on a sphere under arbitrary rotation, Appl. Phys. Lett. 89 (18) (2006).
[73] J.P.F. Campos, K.R.B. Melo, G.C. Lopes, Implementation, validation and application of a lubrication force model in CFD-DEM simulations, Braz. J. Chem. Eng. 39 (2) (2022) 429–440.
[74] I. Tomac, M. Gutierrez, Fluid lubrication effects on particle flow and transport in a channel, Int. J. Multiphase Flow 65 (2014) 143–156.
[75] T.M.J. Nijssen, M. Ottens, J.T. Padding, A note on the modelling of lubrication forces in unresolved simulations, Powder Technol. 413 (2023) 118017.
[76] A. Wachs, L. Girolami, G. Vinay, G. Ferrer, Grains3D, a flexible DEM approach for particles of arbitrary convex shape – Part I: numerical model and validations, Powder Technol 224 (2012) 374–389.
[77] Z. Lai, S. Zhao, J. Zhao, L. Huang, Revisiting the GJK and shape erosion method for contact resolution in DEM, Powder Technol. 394 (2021) 363–371.
[78] H. Jasak, A. Jemcov, Z. Tukovic, et al., OpenFOAM: a C + + library for complex physics simulations, in: International Workshop on Coupled Methods in Numerical Dynamics, 1000, IUC Dubrovnik Croatia, 2007, pp. 1–20.
[79] W. Jakob, J. Rhinelander, D. Moldovan, Pybind11–seamless operability between c + + 11 and python, 2017, https://github.com/pybind/pybind11 (2019).
[80] R. Di Felice, The voidage function for fluid-particle interaction systems, Int. J. Multiphase Flow 20 (1) (1994) 153–159.

[81] D. Gidaspow, Multiphase flow and fluidization: continuum and kinetic theory descriptions, Academic press, 1994.

[82] D.L. Koch, R.J. Hill, Inertial effects in suspension and porous-media flows, Annu. Rev. Fluid Mech. 33 (1) (2001) 619–647.

[83] C.A. De Moura, C.S. Kubrusly, The Courant–Friedrichs–Lewy (CFL) condition, AMC 10 (12) (2013) 45–90.

[84] H. Dütsch, F. Durst, S. Becker, H. Lienhart, Low-Reynolds-number flow around an oscillating circular cylinder at low Keulegan–Carpenter numbers, J. Fluid Mech. 360 (1998) 249–271.

[85] R. Zhao, O. Faltinsen, J. Aarsnes, Water entry of arbitrary two-dimensional sections with and without flow separation, in: Proceedings of the 21st Symposium on Naval Hydrodynamics, 1996, pp. 408–423.

[86] Y. Di, L. Zhao, J. Mao, E. Avital, A resolved CFD-DEM-IBM algorithm for water entry problems, Ocean Eng. 240 (2021) 110014.

[87] A. ten Cate, C.H. Nieuwstad, J.J. Derksen, H.E.A. Van den Akker, Particle imaging velocimetry experiments and lattice-Boltzmann simulations on a single sphere settling under gravity, Phys. Fluids 14 (11) (2002) 4012–4025.

[88] S.P. Pudasaini, A fully analytical model for virtual mass force in mixture flows, Int. J. Multiphase Flow 113 (2019) 142–152.

[89] L.-T. Sheng, S.-S. Hsiau, N.-W. Hsu, Experimental study of the dynamic behavior and segregation of density-bidisperse granular sliding masses at the laboratory scale, Landslides 18 (2021) 2095–2110.

[90] Y. Kong, M. Guan, X. Li, J. Zhao, H. Yan, How flexible, slit and rigid barriers mitigate two-phase geophysical mass flows: a numerical appraisal, J. Geophys. Res. Earth Surf. 127 (6) (2022) e2021JF006587.

[91] H. Vicari, Q.-A. Tran, M.M. Juel, J. Gaume, The role of dilatancy and permeability of erodible wet bed sediments in affecting erosion and runout of a granular flow: two-phase MPM–CFD simulations, Comput. Geotech. 185 (2025) 107307.

[92] M. Robbe-Saule, C. Morize, R. Henaff, Y. Bertho, A. Sauret, P. Gondret, Experimental investigation of tsunami waves generated by granular collapse into water, J. Fluid Mech. 907 (2021) A11.

[93] E. Deal, J.G. Venditti, S.J. Benavides, R. Bradley, Q. Zhang, K. Kamrin, J.T. Perron, Grain shape effects in bed load sediment transport, Nature 613 (7943) (2023) 298–302.

[94] A. Kubowicz-Grajewska, Experimental investigation into wave interaction with a rubble-mound submerged breakwater (case study), J. Mar. Sci. Technol. 22 (2) (2017) 313–326.

[95] R. Vafaeipour Sorkhabi, A. Naseri, M.T. Alami, A. Mojtahedi, Experimental study of an innovative method to reduce the damage of reshaping rubble mound breakwaters, Innov. Infrastruct. Sol. 7 (6) (2022) 353.